

FINAL REPORT
EMPIRICAL EVALUATION OF
PUMP INLET COMPLIANCE

Contract - NAS 8-27731

DCN 1-1-50 13706 (1F), DCN 1-1-50 13706 (S1) (1F)

Prepared by
F. G. Ghahremani
and
S. Rubin
Vehicle Engineering Division


JULY 1972

Engineering Science Operations
THE AEROSPACE CORPORATION
El Segundo, California

Prepared for
GEORGE C. MARSHALL SPACE FLIGHT CENTER
NATIONAL AERONAUTICS AND SPACE ADMINISTRATION
MARSHALL SPACE FLIGHT CENTER/ALABAMA 35812

FINAL REPORT
EMPIRICAL EVALUATION OF
PUMP INLET COMPLIANCE

Approved by



J. G. Wilder, Jr., Head
Propulsion Department
Aero Engineering Subdivision
Vehicle Engineering Division

FOREWORD

This final report is submitted in accordance with the requirements of the Statement of Work for Contract NAS8-27731, and documents the work accomplished during the contract period, 29 June 1971 through 28 July 1972. This study was performed for the George C. Marshall Space Flight Center of the National Aeronautics and Space Administration, and was administered technically by Mr. Raymond Spink of the Science and Engineering Directorate, Astronautics Laboratory.

ABSTRACT

Pump cavitation compliance represents the hydraulic compressibility of the bubbles formed from the complex cavitation process at pump inlets. Such "bubble" compliance is a significant factor in establishing the resonant frequencies for the dynamics of rocket engines and, as such, must be known for the pogo stability analysis of a launch vehicle.

Cavitation compliance has been determined experimentally from pulsing tests on a number of rocket turbopumps. The primary test data used for this study are those for the Rocketdyne H-1, F-1, and J-2 oxidizer and fuel pumps employed on Saturn vehicles. The study shows that these data can be correlated by a particular form of nondimensionalization, the key feature of which is to divide the operating cavitation number or suction specific speed by its value at head breakdown. A previous study (Ref. 3) concluded that such a correlation was not possible since breakdown information was not employed. An expression is obtained for a best-fit curve for these data. Another set of test data for the Aerojet LR87 and 91 pumps can be correlated by a somewhat different nondimensional pump performance parameter, specifically by relating the cavitation number to its position between the head breakdown point and the point of zero slope of the head coefficient versus cavitation number.

A study of mathematical models for the cavitation compliance correlation shows a degree of success. Involved are an assumption that the bubble volume at any pump operating point is proportional to a power of a nondimensional performance parameter involving a relationship to head breakdown.

Recommendations are given for the estimation of the cavitation compliance for new designs in the Rocketdyne family of pumps.

CONTENTS

FOREWORD	iii
ABSTRACT	iv
SYMBOLS	ix
1. INTRODUCTION	1
1.1 Background	1
1.2 Objective	3
1.3 Scope	3
2. EVALUATION OF DATA	4
2.1 Cavitation Compliance Test Data	4
2.1.1 F-1 Oxidizer Pump Compliance Data	6
2.1.2 J-2 Oxidizer Pump Compliance Data	8
2.1.3 H-1 Fuel Pump Compliance Data	8
2.1.4 LR91 Fuel Pump Compliance Data	8
2.2 Pump Design and Performance Data	9
2.2.1 Cavitation Performance	9
3. EMPIRICAL CORRELATION OF CAVITATION COMPLIANCE DATA	18
4. MATHEMATICAL MODELS OF PUMP CAVITATION COMPLIANCE	24
4.1 Bubble Volume	24
4.1.1 Bubble Volume from Free-Streamline-Wake Theory	24
4.1.2 Empirical Approaches to Bubble Volume	25
4.2 Blade Cavitation Compliance - Mathematical Model	28
4.3 Backflow Cavitation Compliance Theory - Mathematical Model	28

CONTENTS (Continued)

4.3.1	General Discussion of Backflow	28
4.3.2	Pump Performance Related to Backflow	32
4.3.3	Pump Performance Prediction	34
4.3.4	Backflow Flow Rate	35
4.3.5	Velocity Distribution with Backflow	36
4.3.6	Cavitation Compliance with Backflow	36
4.4	Gaseous Cavitation - Mathematical Model	38
5.	EVALUATION OF MATHEMATICAL MODELS	39
5.1	Free-Streamline-Wake Theory for Blade Cavitation Compliance	39
5.2	Results for Cavitation Compliance Considering Backflow.	42
5.3	Results of Empirical Approaches to Blade Cavitation Compliance	48
5.4	Gaseous Cavitation Compliance.	57
5.5	Curve Fitting Equation	57
6.	CONCLUSIONS	60
7.	RECOMMENDATIONS	62
APPENDICES:		
A.	BLADE CAVITATION COMPLIANCE	63
B.	BACKFLOW CAVITATION COMPLIANCE	68
C.	GASEOUS CAVITATION COMPLIANCE	73
	REFERENCES	75

FIGURES

1.	Oxidizer and Fuel Pumps Cavitation Compliance	5
2.	F-1 Oxidizer Pump Cavitation Compliance and PVC Compliance Versus Pressure	7
3.	Inducer Leading-Edge Blade Angle Distribution for Rocketdyne Pumps	11
4.	Dimensionless Presentation of Pump Cavitation Performance . .	12
5.	Cavitation Number at Breakdown for the Rocketdyne Pumps . . .	14
6.	Cavitation Number at 10 Percent Drop in Head for the Titan Pumps	15
7.	F-1 Oxidizer Pump Cavitation Performance	16
8.	Dimensionless Pump Cavitation Compliance Versus K/K^*	19
9.	Dimensionless Pump Cavitation Compliance Versus S/S^*	21
10.	Dimensionless Pump Cavitation Compliance Versus $(K-K^*)/K_I-K^*$	22
11.	Sketch of Partly Cavitating Cascade	25
12.	Bubble Area at Cavitation Breakdown	26
13.	Relative Circulation Within an Impeller Channel	31
14.	Indicated Backflow in the LR87 Fuel Pump	31
15.	Assumed Backflow Velocity Distribution at the Inducer Inlet. . .	37
16.	Test Versus Blade Cavitation Prediction Using Free- Streamline-Wake Theory	40
17.	Test Versus Blade Cavitation Prediction Using Free- Streamline-Wake Theory With K_{Mod}	41
18.	Test Versus Backflow Cavitation Prediction With $(K^*/K)^{0.5}$ and $\tau = 1$	43

FIGURES (Continued)

19.	Test Versus Backflow Cavitation Prediction With $(K^*/K)^{0.5}$ and $\tau = 1$	45
20.	Test Versus Backflow Cavitation Prediction With $(S/S^*)^{0.5}$ and $\tau = 1$	46
21.	Test Versus Backflow Cavitation Prediction With $(S/S^*)^{0.2}$ and $\tau = 1$	47
22.	Test Versus Blade Cavitation Prediction With $(S/S^*)^{0.2}$ and $\tau = 1$	51
23.	Test Versus Blade Cavitation Prediction With $(S/S^*)^{0.2}$ and $t = 4.8$ msec	53
24.	Test Versus Blade Cavitation Prediction With $[(K_I - K^*)/(K - K^*)]^{0.15}$ and $\tau = 1$	55
25.	Test Versus Blade Cavitation Prediction With $[(K_I - K^*)/(K - K^*)]^{0.15}$ and $t = 4.8$ msec	56
26.	Predicted Total Compliance With a Gas Content of $X_G = 0.01$ Percent	58
27.	Comparison Between Test Results and Best Curve Fitting . . .	59
28.	Velocity Triangle for the Backflow Region	69

TABLES

I.	Design and Performance Data for Rocket Engine Pumps	10
II.	Pump Performance Prediction Parameters	33

SYMBOLS*

A	area, m^2 , $in.^2$
C_b	cavitation compliance, m^2 , $in.^2$
C_L	backflow absolute velocity, m/sec, ft/sec
C_m	axial component of the absolute velocity, m/sec, ft/sec
C_u	whirl component of absolute velocity, m/sec, ft/sec
c	length of vapor cavity, m, in.
D	impeller diameter, m, in.
d	blade spacing, $2 \pi r/z$, m, in.
g	gravitational constant 9.807 m/sec^2 , 32.2 ft/sec^2
h	cavity height at cavity closure, m, in.
K	cavitation number
K_I	cavitation number at zero slope of ψ versus K curve
L	ratio of backflow to through flow
M	mass, Kg, $lb\text{-sec}^2/ft$
N	pump rotational speed, revolution per sec, revolution per min (rpm)
N_S	pump specific speed, dimensionless, $\text{rpm} \sqrt{\text{gpm}}/(\text{ft})^{3/4}$
n	empirical exponent
NPSH	Net Positive Suction Head, Joules/Kg, ft
P_s	static pressure, Newton/m^2 , psia
P_v	vapor pressure, Newton/m^2 , psia

*In describing each symbol the unit immediately following the description is in SI units followed by the conventional engineering units.

SYMBOLS (Continued)

Q_0	volumetric flow, m^3/sec , ft^3/sec
R	gas constant, Joules/Kg $^{\circ}$ Kelvin, ft-lb/lb $^{\circ}$ R
r	radius, m, in.
r_{ia}	lower radius, backflow region, m, in.
S	suction specific speed, dimensionless, $rpm \sqrt{gpm}/(ft)^{3/4}$
T	temperature, $^{\circ}$ Kelvin, $^{\circ}$ Rankine
t	stay time of the bubble, sec
U	tangential velocity, m/sec, ft/sec
V	volume, m^3 , $in.^3$
W	relative velocity, m/sec, ft/sec
X_G	mass fraction of gas in liquid at the pump inlet
z	number of blades, inducer
α	inducer inlet incidence angle, $\alpha = \beta - \beta_F$, Radian, deg
β	inducer inlet blade angle with respect to tangent, Radian, deg
β_F	inducer inlet relative velocity angle, Radian, deg
γ	the angle measured between the tangent and the tip circular arc at the impeller discharge and the axis of rotation, Radian, deg
Δ	diffusion factor
Δh	pump head rise, Joule/Kg, ft
$\Delta\psi$	head loss coefficient
ϵ	impeller diameter ratio, r_i/r_t
η	pump efficiency

SYMBOLS (Continued)

μ	slip factor
ρ	density, Kg/m ³ , lb/ft ³
θ	backflow velocity absolute angle, Radian, deg
\emptyset	flow coefficient
τ	solidity
ψ	head coefficient, $\Delta h / (U_t^2 / g)$
ψ_T	total head coefficient, ψ / η
ψ_{Th}	actual Euler head coefficient
ψ_{∞}	ideal Euler head coefficient

Subscripts

B	backflow
b	bubble
c	quantities evaluated on free streamline
Ext	External
G	gas
h	inducer inlet hub
i	inducer inlet eye
j	any station along the radius
L	liquid
1	inducer inlet, upstream
2	inside inducer at wake collapse

SYMBOLS (Concluded)

m	mean
s	static
T	total
t	impeller tip

Superscript

*	at cavitation breakdown
---	-------------------------

1. INTRODUCTION

1.1 BACKGROUND

Longitudinal structural oscillations and corresponding propellant oscillations at frequencies in the range of 5 to 60 Hz, referred to as pogo, have been observed to erupt spontaneously on a number of liquid propellant launch vehicles during powered flight (Ref. 1). Pogo results from an unstable dynamic interaction of the vehicle (structure and tanks) with the propulsion system (engines and feedlines). The propulsion system displays resonant characteristics as a result of hydraulic resonances of the feedlines. The relationship of the frequencies of feedline resonances to the natural frequencies of the vehicle structure is a major factor for system stability. A feedline resonant frequency can be significantly affected by (1) pump cavitation compliance, (2) the structural or hydraulic compliance of devices such as accumulators or pressure-volume compensators, and (3) the distributed compliance along the feedline due to propellant compressibility and pipe-wall radial elasticity. Cavitation compliance is defined as

$$C_b = - \frac{dV_b}{dP_s} \rho_L g$$

i.e., the product of the volumetric compliance (negative rate of volume change per unit pressure) and propellant weight density; its units are meters², and in engineering units, inches². Pump cavitation compliance represents the hydraulic compressibility associated with bubbles formed from the complex cavitation process at pump inlets. These bubbles have been observed in flow-visualization studies, and this bubble compliance must be known for the pogo stability analysis of a launch vehicle.

Pump cavitation compliance could be determined directly by measuring oscillatory flow both upstream and downstream of the cavitation region in conjunction with oscillatory pump-inlet pressure measurement. This has generally not been possible because of the unavailability of dynamic flowmeters.

As a result the cavitation compliances must be inferred via a less direct means. Often the inference is based on the pump-inlet compliance required to yield an observed resonant frequency based on a mathematical model of the particular test or flight configuration. Obviously, the result can reflect errors resulting from any misrepresentation in the system. All the cavitation compliance data used in this study is subject to uncertainty resulting from such error. Some of these uncertainties are noted and discussed in Ref. 3*. For purposes of this study, only the best estimates of the cavitation compliances are employed.

An earlier empirical study of the cavitation compliance of Aerojet pumps used on Titan vehicles was conducted by Ghahremani (Ref. 2). That study concluded that the compliance is primarily the result of backflow (recirculation to the pump inlet of high-pressure flow past the tip of the unshrouded impeller) and not the result of cavitation actually attached to the inducer blades. The result of that study was a partial agreement between an empirical model and the experimental data.

A more recent study was conducted by Martin Marietta Corporation (Ref. 3) using the same Saturn vehicle pumps and Titan pumps that are considered in this study. The main emphasis of that study was to develop an analytical model using a potential flow solution to determine cavitation compliance by calculating vapor volume between the pump blades caused by blade cavitation. Gaseous cavitation, and cavitation resulting from flow recirculated to the pump inlet were not treated. A computer program was developed and applied to the following oxidizer pumps: J-2, F-1, and H-1 Saturn pumps and the LR87 Titan pump. The analytical method predicted much less cavitation compliance than the test data indicates. The results were quite disappointing, with no cavitation (or practically none) predicted for the F-1,

* Not mentioned in Ref. 3 is the possible importance of pump dynamic gain in deriving cavitation compliance. In a current study of the Thor/Delta Vehicle and its MB-3 engine, we have recently found that pump dynamic gain (partial derivative of head rise with respect to inlet pressure, Ref. 1) can substantially influence the resonant frequency of a feedline/engine system. It would be worthwhile to review the various determinations of cavitation compliance to determine how the pump gain was considered.

H-1, and LR87 pumps. It was concluded that mechanisms other than blade cavitation must predominate. An empirical study of the data, in Ref. 3, led to the additional conclusion that a nondimensional combination of pump geometry and fluid properties could not be found to correlate the available test data.

1.2 OBJECTIVE

The objective of this study was to develop an empirical method which relates the F-1, J-2, and H-1 pump-inlet cavitation compliance to turbo-pump design geometry, performance characteristics and fluid properties. The empirical model, as developed, could be used for the prediction of the cavitation compliance for new designs of this class of pumps in advance of experimental determinations. Such prediction should improve the quality of preliminary pogo stability analysis of new vehicles such as the Space Shuttle.

1.3 SCOPE

This study was primarily concerned with the prediction of cavitation compliance for the F-1, J-2, and H-1 pumps operating at their normal speed under flow conditions for which the compliance data were available. The study considered normal blade cavitation, backflow cavitation, and their effect on compliance. In addition to the Saturn pumps, Titan pumps were also studied as an aid to understanding pump design effects.

2. EVALUATION OF DATA

2.1 CAVITATION COMPLIANCE TEST DATA

The cavitation compliance data as a function of cavitation number at the inducer eye is shown in Fig. 1 and is based upon Fig. 4-21* of Ref. 3. Cavitation number at the inducer eye is a dimensionless parameter defined as**

$$K_i = \left(P_s - P_v \right) / \frac{\rho_L W_i^2}{2} \quad (2-1)$$

where

$$P_s - P_v = \rho_L \left(\text{NPSH} - \frac{C_m^2}{2} \right) \quad (2-2)$$

Substituting Eq. (2-2) into Eq. (2-1), we obtain

$$K_i = \frac{\text{NPSH} - \frac{C_m^2}{2}}{\frac{W_i^2}{2}} \quad (2-3)$$

Assuming no prewhirl at the reducer inlet

$$W_i^2 = U_i^2 + C_m^2 \quad (2-4)$$

*Omitted is data for the MB-3 pumps. Our current investigations of pogo on Thor/Delta vehicles have shown that the MB-3 fuel pump data is invalid, and the oxidizer pump data requires further study.

**To comply with the contractual requirements of this study, all the derivations are in SI units unless otherwise specified.

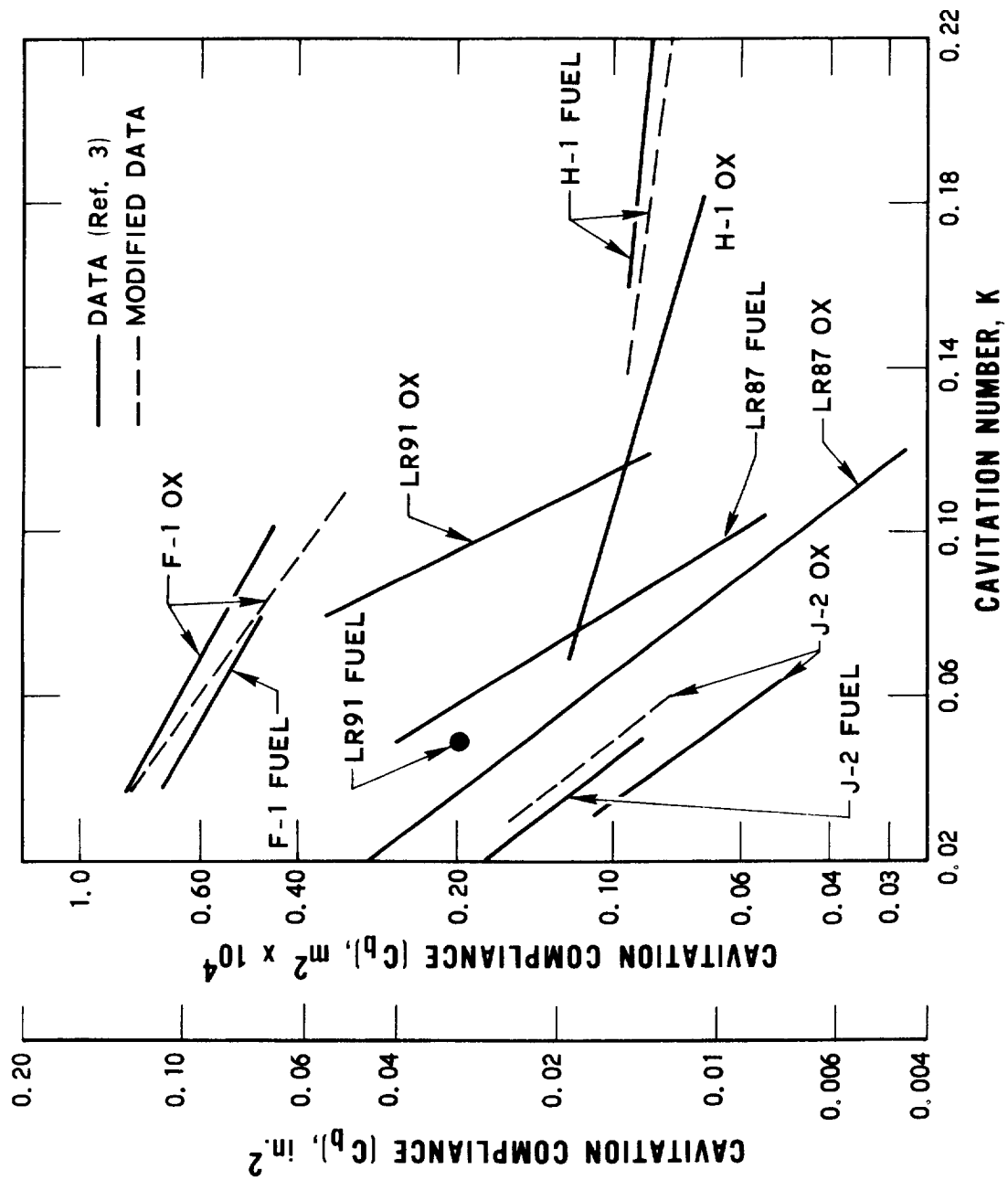


Fig. 1. Oxidizer and Fuel Pumps Cavitation Compliance

and employing the flow coefficient

$$\phi_1 = \frac{C_m}{U_i}$$

we obtain from Eq. (2-3) the desired form

$$K_i = \left(\frac{NPSH}{U_i^2/2} - \phi_1^2 \right) / (1 + \phi_1^2) \quad (2-5)$$

For use in our studies, modifications of the F-1 oxidizer, J-2 oxidizer, and H-1 fuel data are made as shown by the dotted curves. These modifications are discussed in the following text.

2.1.1 F-1 Oxidizer Pump Compliance Data

The solid curves in Fig. 2a (from Fig. 4.9 of Ref. 3) display uncertainty in the cavitation compliance of the F-1 oxidizer pump resulting from differences in alternative determinations of the compliance of a pressure-volume compensator (PVC). The corresponding PVC compliances are shown in Fig. 2b (from Fig. 4.7 of Ref. 3). The cavitation compliance is determined by subtracting the PVC compliance from the overall compliance as inferred from an observed resonant frequency during operation of the pump. On the one hand, non-flow feedline dynamic tests indicate a PVC compliance which decreases rapidly with static pressure. However, static pressure testing of the PVC itself indicates a more constant compliance with pressure, although compliance is reduced by mechanical nonlinearity at pressures above 0.7 MN/m^2 absolute (100 psia); see Figs. 4.4 and 4.5 of Ref. 3. It is concluded in Ref. 3 that the best estimate of PVC compliance lies between the variable and constant estimates (see dotted curve in Fig. 2b). In our opinion the PVC compliance, shown by the dashed curve in Fig. 2b, is a more reasonable estimate and this is the basis for the dashed curve in Fig. 2a, and for the dashed curve of the F-1 oxidizer pump in Fig. 1.

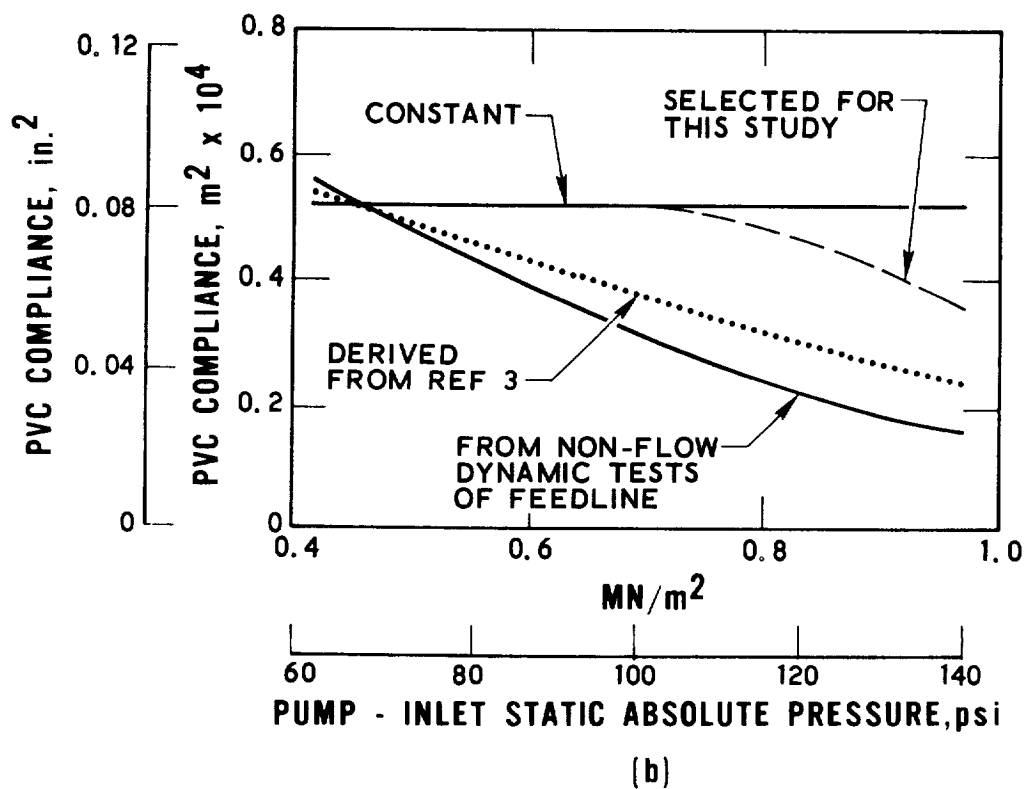
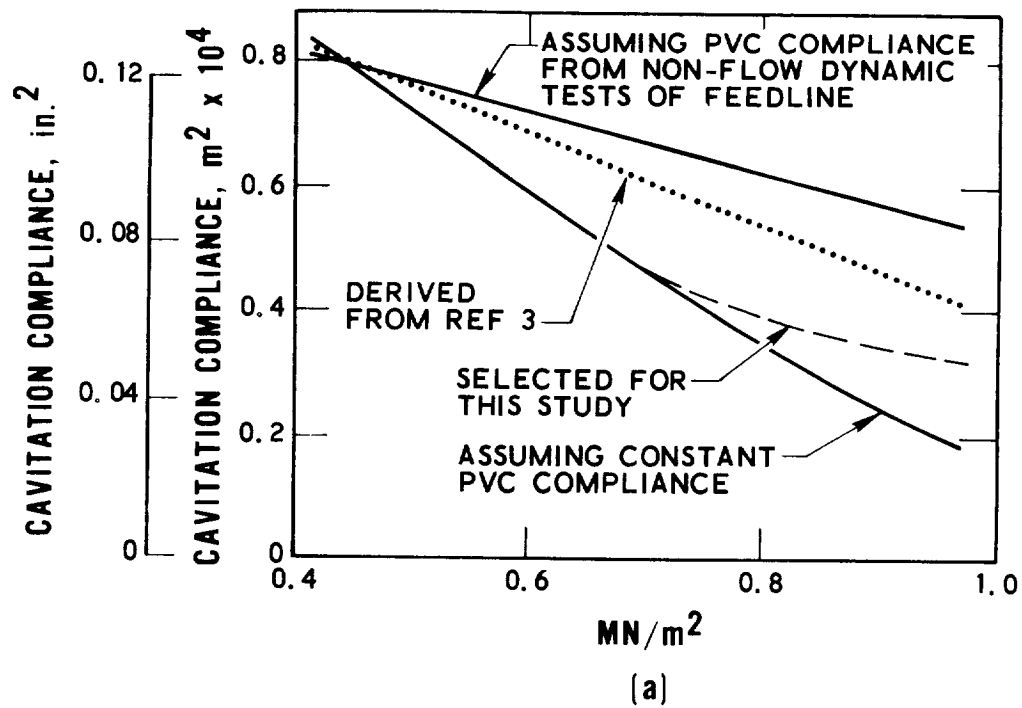


Fig. 2. F-1 Oxidizer Pump Cavitation Compliance and PVC Compliance Versus Pressure

2.1.2 J-2 Oxidizer Pump Compliance Data

Figure 4.16 of Ref. 3 shows a large discrepancy in the results of independent evaluations of the test data from several facilities to derive cavitation compliance. Brown Engineering employed a single-compliance pump model to analyze data from S-II and S-IVB feed system tests. Rocketdyne employed a double-compliance model to analyze their test facility results. Reference 3 states that the results are consistent insofar as resonant frequency is concerned, but produce different cavitation compliance results because of the two types of pump models. Reference 3 rates the Rocketdyne model as the better one, but states that the true cavitation compliance can lie anywhere between the two results. In our conversion of the Brown and Rocketdyne compliances versus inlet static pressure, to versus cavitation number, we find that the curve in Fig. 4.21 of Ref. 3 is nearly equal to the Brown results rather than being an intermediate result. For our purposes, we have elected to use the more reliable Rocketdyne result and this is shown by the dashed curve for the J-2 oxidizer pump in Fig. 1.

2.1.3 H-1 Fuel Pump Compliance Data

Reference 3 employs an erroneous value for the inducer-eye diameter of the H-1 fuel pump, using instead of the large inlet diameter the smaller diameter at the tip of the inducer discharge. The dotted curve for the H-1 fuel pump in Fig. 1 is based on the use of the correct diameter to establish the cavitation number.

2.1.4 LR91 Fuel Pump Compliance Data

Compliance data for the LR91 (Titan Stage II) fuel pump, obtained from feedline resonance observed in flight, is limited to a single NPSH. It appeared initially that recent static firing tests would provide Stage II fuel pump data over a wide range of NPSH and would extend the oxidizer pump data over a much wider range of NPSH than available from flight. Oscillographic pump-inlet pressure data were obtained from Aerojet and reviewed visually in an attempt to identify feedline resonant frequency versus NPSH.

Unfortunately, feedline resonant frequencies could not be detected and this search for additional Titan data was discontinued.

2.2 PUMP DESIGN AND PERFORMANCE DATA

Two sources of pump performance and design data were used in this study. Initially, the work in Ref. 3 was available and then further data were obtained from Rocketdyne. The Rocketdyne data are presented in Table I, together with similar Titan data which were obtained from Refs. 2 and 4. The pump data in Ref. 2 were based on pump tests without prevalves upstream of the pumps, whereas the data shown in Ref. 4 were based on pump tests with prevalves. Prevalves are used in the flight vehicle and they have a substantial effect on the pump performance because of the high backflow of these pumps.

In addition to the data shown in Table I, the leading-edge blade-angle distributions for F-1, J-2, and H-1 pumps were received from Rocketdyne and are presented in Fig. 3. For the Titan pumps, it is assumed that the leading-edge blade-angle distribution is that of a radial element

$$r \tan \beta = \text{Constant} \quad (2-6)$$

where r is the radial distance from axis of rotation and β the leading-edge blade angle.

2.2.1 Cavitation Performance

In general, the dimensionless cavitation performance of a pump can be presented in terms of head coefficient (ψ) versus cavitation number (K) for a fixed flow coefficient (ϕ_1) as shown in Fig. 4. At high K values, the slope of the curve is zero and as K is reduced to K_T , the slope begins to change. As K is reduced further to K^* , the head breaks down and the slope of the curve becomes infinite. The cavitation performance data were used

Table I. Design and Performance Data for Rocket Engine Pumps

Pump Design	Stage I Titan (LR87)		Stage II Titan (LR91)		F-1		F-2		H-1	
	Fuel	Oxidizer	Fuel	Oxidizer	Fuel	Oxidizer	Fuel	Oxidizer	Fuel	Oxidizer
Impeller Diam, m (in.)	0.2751 (10.75)	0.2343 (9.22)	0.1251 (4.92)	0.2221 (8.74)	0.5804 (22.85)	0.4953 (19.50)	-----	0.5541 (21.82)	0.3302 (13.0)	0.2751 (10.8)
Inducer Eye Diam, m (in.)	0.1685 (6.63)	0.1803 (7.10)	0.0902 (3.55)	0.1294 (5.09)	0.3990 (15.71)	0.4001 (15.75)	0.198 (7.8)	0.1715 (6.75)	0.1714 (6.75)	0.1930 (7.6)
Impeller Tip Width, m (in.)	0.0188 (0.74)	0.0254 (1.0)	0.0112 (0.44)	0.0127 (0.50)	0.0384 (1.51)	0.0360 (1.41)	-----	0.0193 (0.76)	0.0203 (0.8)	0.0273 (1.1)
Inducer Inlet Area, m ² (in. ²)	0.0192 (29.8)	0.0231 (35.8)	0.0069 (10.7)	0.0116 (18)	0.1030 (159.6)	0.1193 (185)	0.0204 (41.0)	0.0221 (34.3)	0.021 (32.6)	0.0273 (42.3)
Inducer Blade Angle at Eye, Rad (deg)	0.0995 (5.7)	0.0995 (5.7)	0.0995 (5.7)	0.0995 (5.7)	0.131 (7.5)	0.147 (8)	0.1222 (7.0)	0.114 (10)	0.1675 (9.4)	0.2123 (11.4)
Impeller Tip Angle, Rad (deg)	0.6108 (35)	0.4886 (28)	0.4886 (28)	0.6108 (35)	0.4363 (25)	0.631 (38)	-----	0.4712 (27)	0.5235 (30)	0.5235 (30)
Number of Blades, Impeller Tip	12	9	8	12	6	6	-----	6	16	16
Number of Blades, Inducer	3	3	3	3	4	3	4	3	4	4
Tip Clearance, m (in.)	0.00114 (0.045)	0.00114 (0.045)	0.00114 (0.045)	0.00114 (0.045)	0.00114 (0.045)	0.00114 (0.045)	-----	0.00114 (0.045)	0.00114 (0.045)	0.00114 (0.045)
Performance										
Propellant	A-50	N ₂ O ₄	A-50	N ₂ O ₄	RP-1	LOX	LiH ₂	LOX	RP-1	LOX
Q Flow, m ³ /sec (gpm)	0.135 (2141)	0.1626 (2580)	0.0578 (918)	0.0607 (963)	0.956 (1517)	1.50 (2380)	0.5027 (7980)	0.1537 (2440)	0.1368 (2172)	0.2040 (3252)
Δh, Pump Head m (ft)	1051.5 (3450)	560.8 (1840)	990.5 (3250)	545.5 (1790)	1603 (5260)	1011.8 (3320)	9875.5 (32400)	543.4 (1783)	847.3 (2780)	583.7 (1915)
N, Rotational Speed, rps (rpm)	153 (9175)	139 (8350)	393 (23575)	139 (8366)	92.5 (5550)	92.5 (5550)	426.7 (25600)	134 (8050)	112.5 (6750)	112.5 (6750)
NS, Specific Speed, Non-Dim, [rpm√gpm/(ft) ^{3/4}]	0.055 (943)	0.088 (1510)	0.0966 (1659)	0.055 (943)	0.0636 (1090)	0.1142 (1958)	-----	0.0846 (1450)	0.0479 (821)	0.0776 (1331)
η, Efficiency Percent	68.4	72.5	61.3	68	71	70	73.2	67.5	72	76.5
U ₁ , Impeller Tip Speed, m/sec (ft/sec)	131.4 (431)	104.2 (342)	157.3 (516)	96.77 (317.5)	168.8 (553)	144.1 (472)	-----	109 (358)	117.6 (382.7)	147.32 (481.3)
U ₂ , Inducer Tip Speed, m/sec (ft/sec)	81.1 (266)	78.6 (258)	118.9 (390)	56.4 (185)	116.1 (380)	116.3 (381)	265.5 (871)	72.4 (237)	60.3 (198)	68.35 (224)
Q ₁ , Inducer Inlet Flow Coefficient	0.084	0.089	0.070	0.093	0.081	0.109	0.072	0.097	0.108	0.11
Q ₂ , Impeller Tip Flow Coefficient	0.075	0.096	0.094	0.0835	0.0955	0.1187	-----	0.121	0.065	0.1030
ψ, Head Coefficient	0.598	0.507	0.393	0.572	0.564	0.48	-----	0.448	0.61	0.60
ψ _T , Total Head Coefficient	0.874	0.70	0.641	0.84	0.795	0.686	-----	0.664	0.848	0.784
K ₁ , Cavitation Number at Breakdown:	0.0405	0.029	0.025	0.042	0.0137	0.0136	-----	0.0202	0.026	0.0248
Water	NA	NA	NA	NA	0.0132	0.0077	0.00177	0.0093	NA	0.014
Propellant	NA	NA	NA	NA	0.0302	0.03	0.00665	0.01773	0.081	0.076
K ₂ , Cavitation Number at Zero Slope	0.045	0.132	0.093	0.191	0.0302	0.03	0.00665	0.01773	0.081	0.076

Notes: (1) Performance data apply to the test conditions for which cavitation compliance was determined.
 (2) All pumps are centrifugal except for the axial F-2 fuel pump.
 (3) NA indicates "not available"
 (4) K₁ for the LR87 and LR91 pumps is based on the presence of the vehicle prevalue.

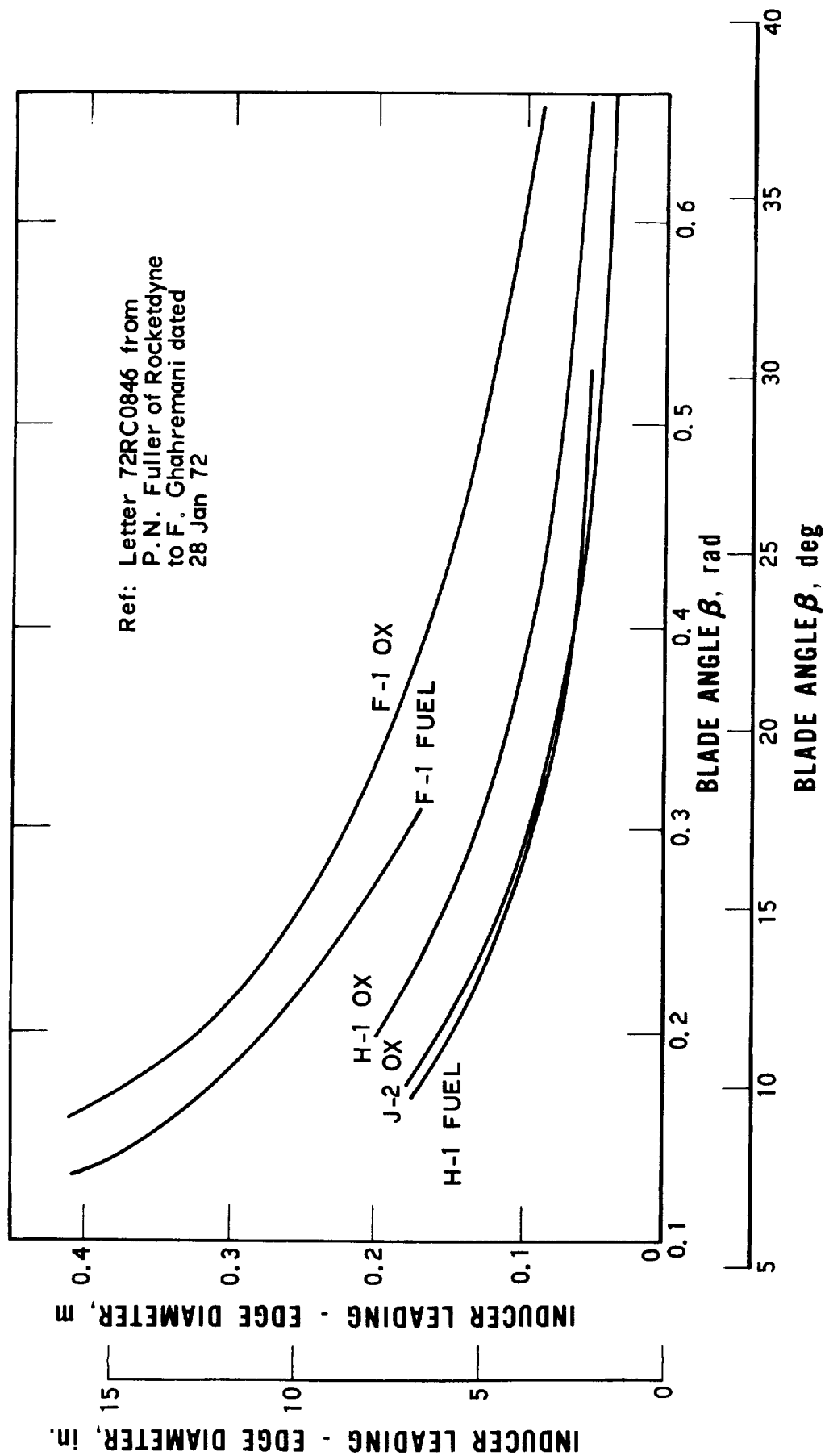


Fig. 3. Inducer Leading-Edge Blade Angle Distribution for Rocketdyne Pumps

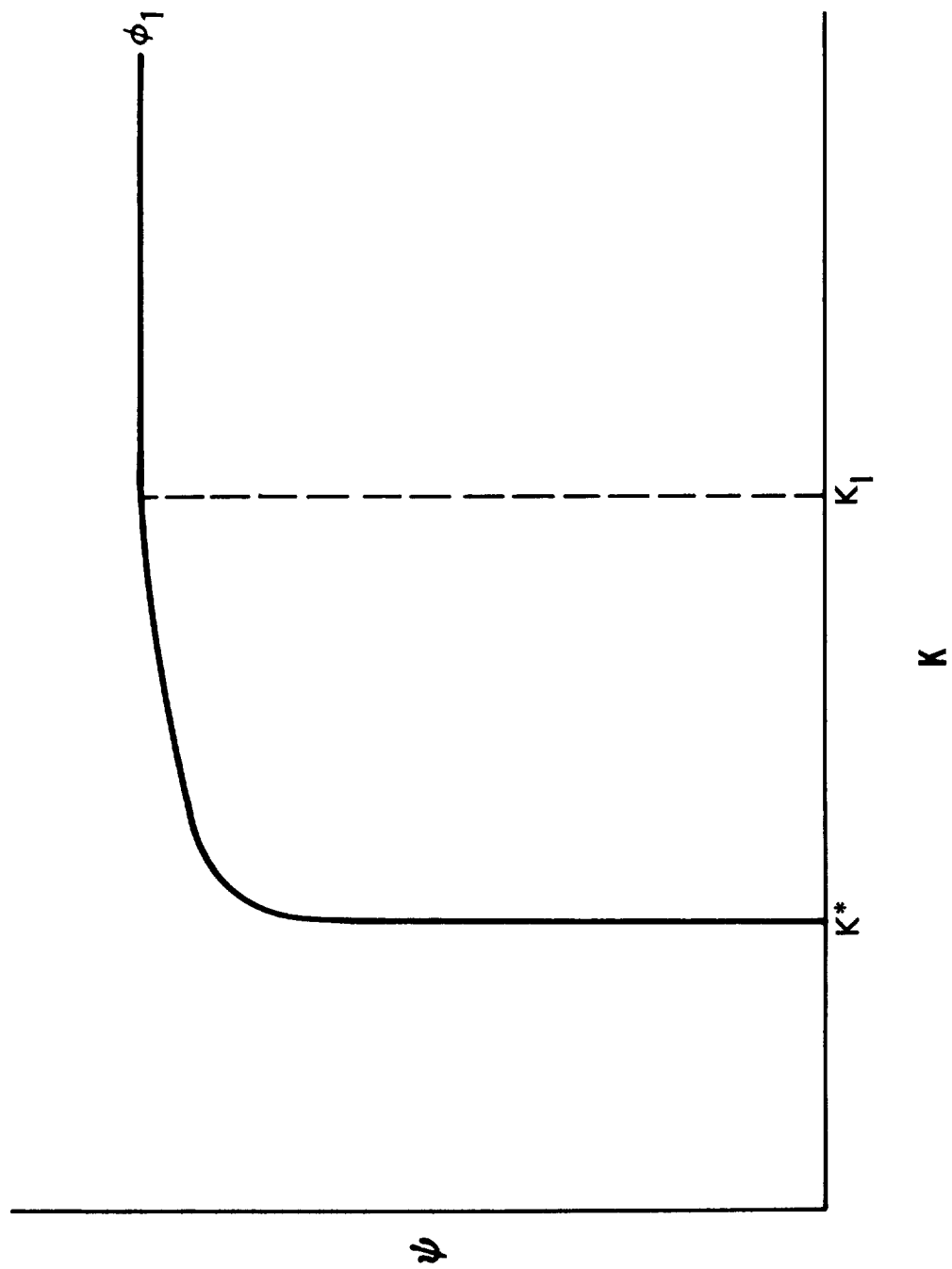


Fig. 4. Dimensionless Presentation of Pump Cavitation Performance

to establish the head-breakdown cavitation number (K^*) for each pump as a function of the pump-inlet flow coefficient (ϕ_1) where

$$K^* = \left(\frac{\text{NPSH}^*}{U_i^2/2g} - \phi_1^2 \right) / \left(1 + \phi_1^2 \right) \quad (2-7)$$

$$\phi_1 = C_m/U_i \quad (2-8)$$

where NPSH* = Net Positive Suction Head at cavitation head breakdown in m(ft). The performance curves received from Rocketdyne[§] and Ref. 4 were used for the calculation of K^* . The data are shown in Figs. 5 and 6 for the Rocketdyne and Titan pumps, respectively. Figure 5 shows the results of several tests using inducers alone, model pumps, and full-scale pumps. All were tested with water, except for the full-scale J-2 fuel pump. All full-scale pumps were tested with propellant, except for the H-1 fuel pump.

The NPSH* values used to calculate K^* were determined from pump performance data such as that presented in Fig. 7, which shows the cavitation performance of the F-1 oxidizer pump. For a value of about 95 percent of the non-cavitating head, the slope is practically infinite. Figure 5 shows the K^* values determined at the point where the slope of head versus NPSH is essentially infinite. For the F-1, J-2, and H-1 pumps this occurs at values between 90 and 95 percent of the non-cavitating head, the precise value being difficult to establish because of the extreme sensitivity to data accuracy. For uniformity, Fig. 5 is based on 95 percent of non-cavitating head for these pumps. Again for uniformity, 90 percent of non-cavitating head for the Titan pumps was arbitrarily selected to determine the K^* shown in Fig. 6, since data were not available at larger head loss for one of the pumps. When data were available, the head loss required to reach infinite slope for the Titan pumps was about 80 percent.

[§]Personal communication by letter 71RC6543 from P.N. Fuller to F.G. Ghahremani, dated 2 September 1971

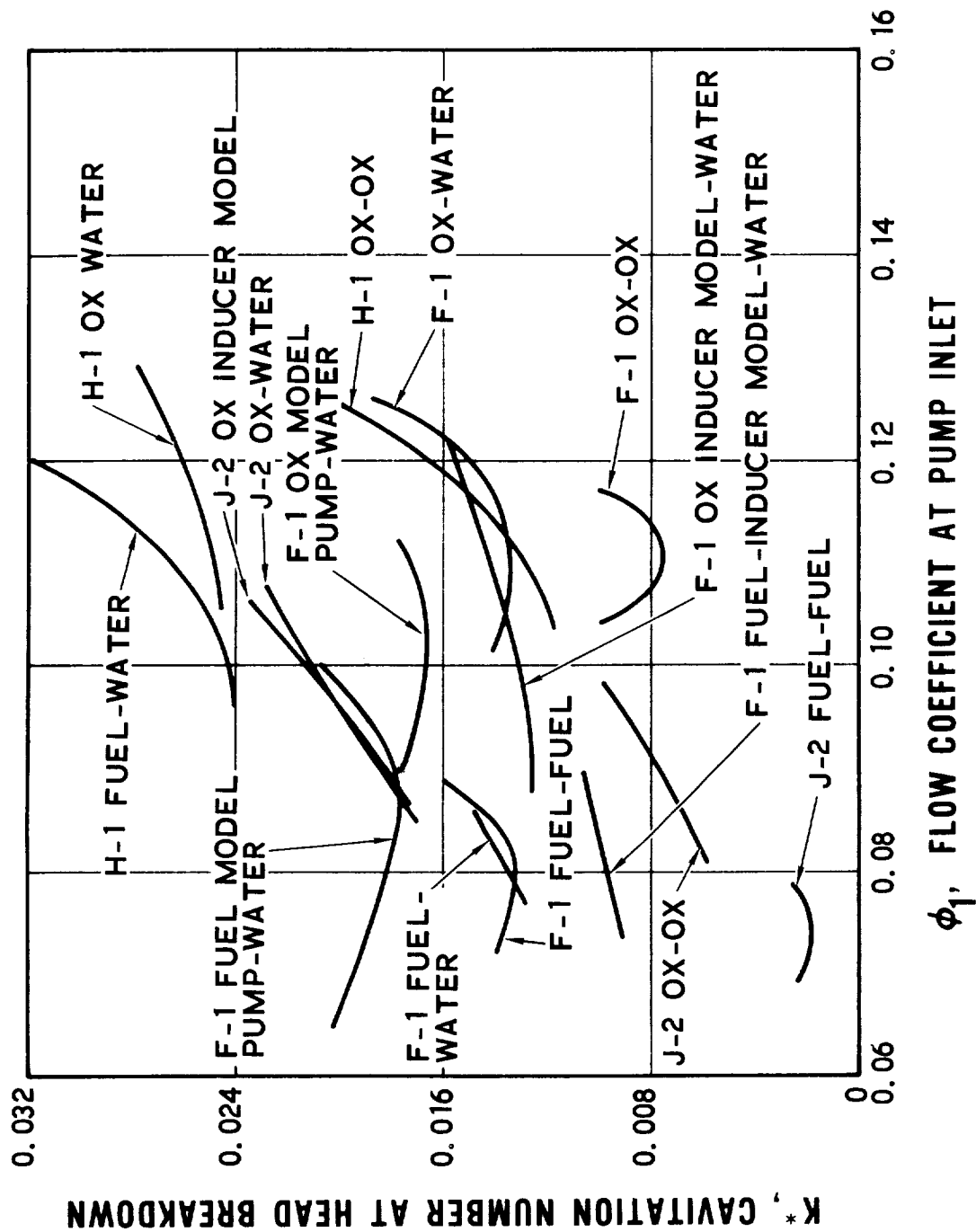


Fig. 5. Cavitation Number at Breakdown for the Rocketdyne Pumps

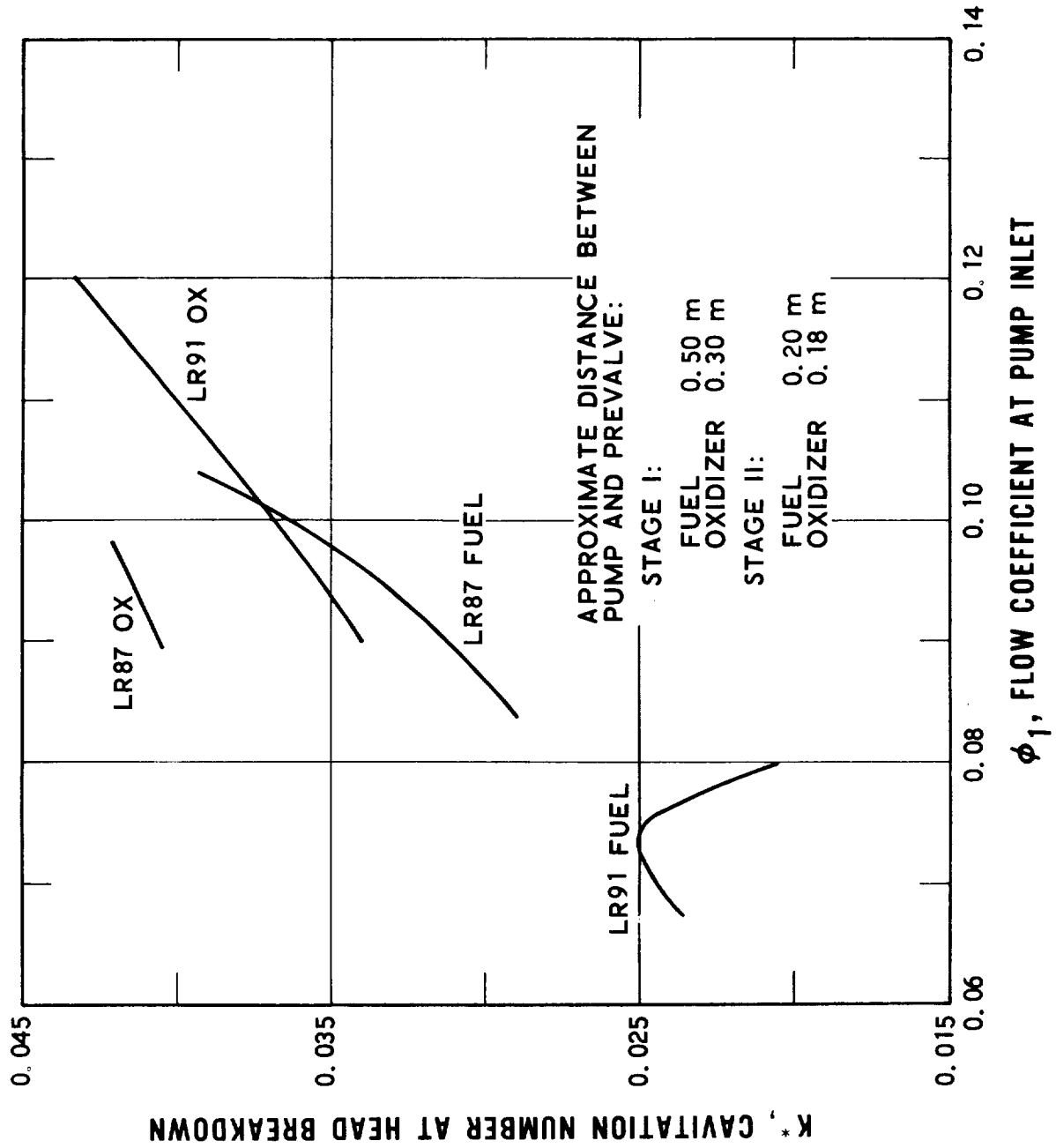


Fig. 6. Cavitation Number at 10 Percent Drop in Head for the Titan Pumps

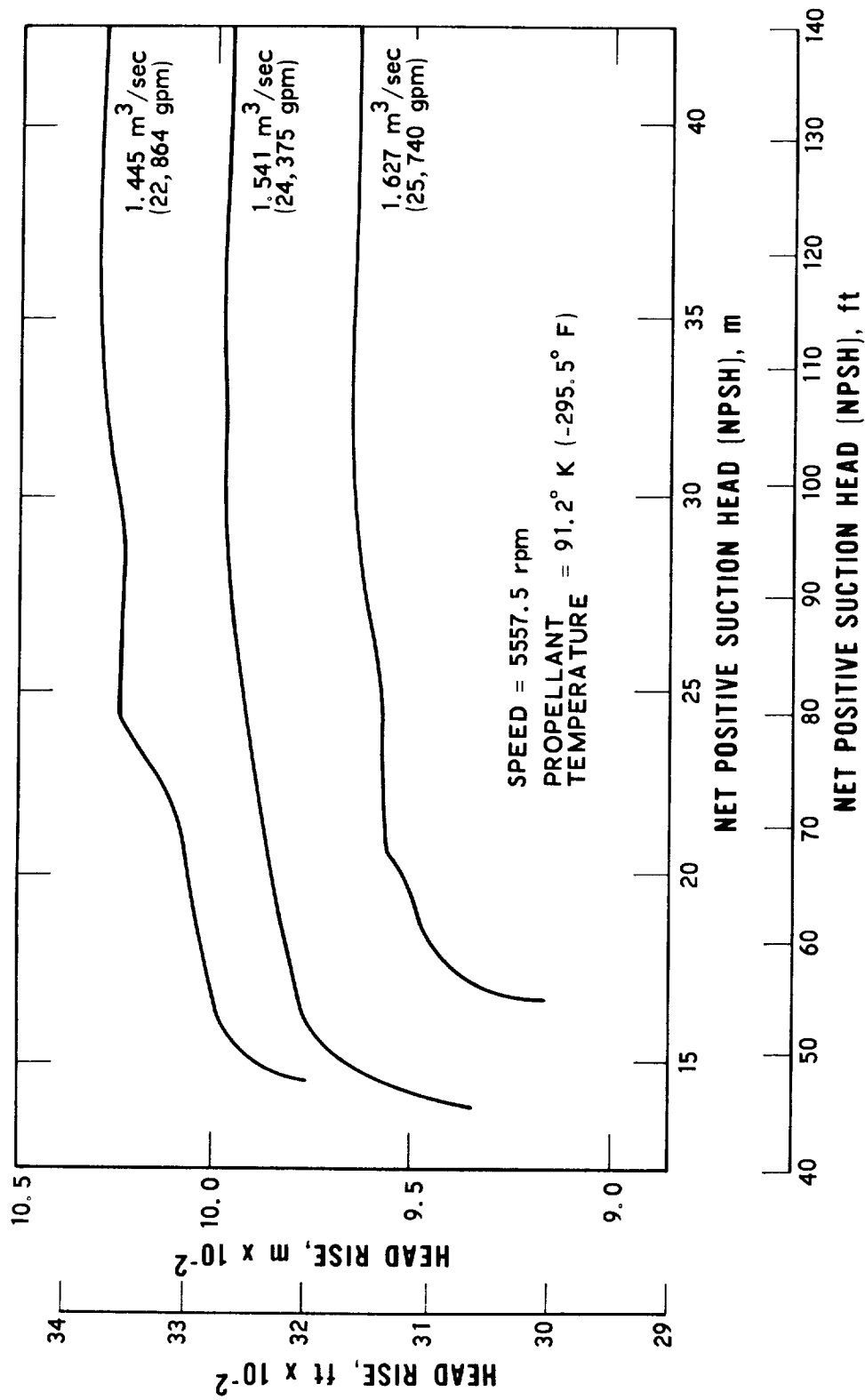


Fig. 7. F-1 Oxidizer Pump Cavitation Performance

The difference between the cavitation performance with water and the propellant is due to an effect called the "thermodynamic suppression head," (TSH). In general, the formation of vapor bubbles requires heat from the surrounding liquid. Therefore, the liquid is cooled as bubbles are formed and the vapor pressure of the liquid is reduced. This depression of the vapor pressure is called TSH. Liquid hydrogen has the highest TSH value (90 to 130 ft of head). Liquid oxygen has values of the order of 5 to 15 ft. RP-1 and Aerozine are known to have negligible TSH. There are indications that N_2O_4 might have some finite TSH value, but no tests have been performed for its determination.

The results shown in Fig. 6 are for the Titan pumps tested with water; both the fuel (Aerozine-50) and the oxidizer (N_2O_4) are assumed to have zero TSH. Note that for the F-1 fuel pump several tests were performed with the inducer alone, with model pumps using water, and with the full-scale pump using both water and RP-1; note also that both the model F-1 oxidizer and fuel pumps tested with water have a higher cavitation number at breakdown than do the full-scale pumps. Furthermore, observe that the F-1 fuel pump tests with water and RP-1 show about the same cavitation performance.

3. EMPIRICAL CORRELATION OF CAVITATION COMPLIANCE DATA

Our attempts to collapse the pump cavitation compliance data by use of pump performance and geometrical information were based on the compliance data presented in Fig. 1, using the dashed curves for the F-1 oxidizer, J-2 oxidizer, and H-1 fuel pumps. These basic data are presented as cavitation compliance C_b in $m^2(in.^2)$ versus cavitation number K . Two unsuccessful attempts were made in Ref. 3 to collapse the curves by non-dimensionalizing the compliance data. In one case, the compliance was divided by the number of inducer blades times the square of the inducer-eye diameter, D_i (see Fig. 4.22 of Ref. 3). In the other case, the D_i^2 was replaced by $(D_i^2 - D_h^2)$, where D_h is the inducer hub diameter, and the reciprocal of the suction specific speed was employed in place of the cavitation number K (see Fig. 4.23 of Ref. 3). In our study we have elected to non-dimensionalize the cavitation compliance by dividing by the pump-inlet area. Moreover, while K is a dimensionless cavitation parameter, other pump performance information is also required to characterize the degree of cavitation. For example, the relationship of the pump operating point to the head breakdown point must also be important. As our first attempt we take the ratio of K/K^* to indicate the cavitation status at the operating point. Figure 8 shows the dimensionless compliance C_b/A_1 versus K/K^* for all the pumps. With the exception of the J-2 fuel pump, the curves for the Rocketdyne pumps collapse rather well. The curves for the Titan pumps exhibit a much steeper slope than do those for the Rocketdyne pumps and are not collapsed by the plotting.

A second possibility is to plot the data versus the ratio S/S^* (ratio of suction specific speeds). In turbomachinery engineering practice, suction specific speed is defined as

$$S = N \sqrt{Q} / (NPSH)^{3/4} \quad (3-1)$$

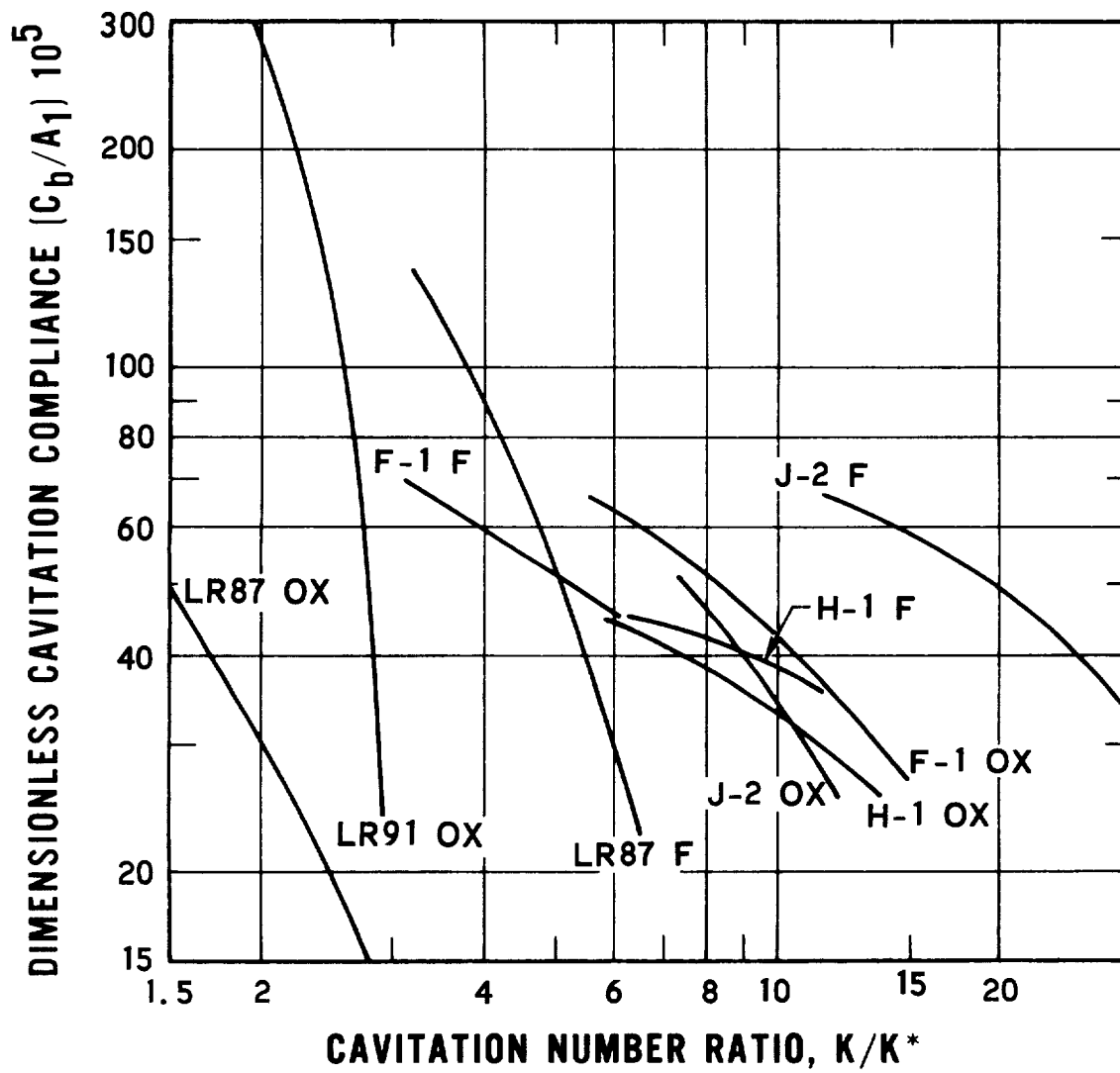


Fig. 8. Dimensionless Pump Cavitation Compliance Versus K/K^*

which is a dimensionless parameter but, by convention, in engineering units Q is in gpm, N is in rpm and NPSH is in ft. For fixed N and Q, we have

$$\frac{S}{S^*} = \left(\frac{NPSH^*}{NPSH} \right)^{3/4} \quad (3-2)$$

Thus, the NPSH ratio would be an equivalent of the S ratio for correlating the data. In terms of K^* and ϕ_1 , we can also write the S ratio as

$$\frac{S}{S^*} = \left[\frac{K^* (1 + \phi_1^2) + \phi_1^2}{K (1 + \phi_1^2) + \phi_1^2} \right]^{3/4} \quad (3-3)$$

Figure 9 shows C_b/A_1 versus S/S^* for all the pumps. Note that the J-2 fuel pump correlates better with the other Saturn pumps as compared to Fig. 8, although the J-2 oxidizer does not. The reason may be that for the J-2 fuel pump K^* is quite uncertain because of the dominance of ϕ_1^2 over K^* , whereas S/S^* is less subject to this uncertainty [see Eq. (3-3)]. The J-2 oxidizer pump has a unique feature in that there is about a 15-percent recirculation of flow from the pump discharge to the inducer discharge. This recirculation pressurizes the inducer discharge and would be expected to inhibit cavitation somewhat. The consequences would be a lower compliance as shown in Fig. 9.

In still another approach, we account for the position of the pump operating point relative to the region of heavy cavitation, where the latter is based on the effect of cavitation on pump performance. This region is considered to extend from the point of head breakdown at K^* to the initial point where the ψ versus K curve has zero slope, denoted by the cavitation number K_I . In this scheme we plot the dimensionless cavitation compliance versus the abscissa $(K-K^*)/(K_I-K^*)$ and the result is shown in Fig. 10. Note that when the abscissa is less than one, pump operation is within the region of

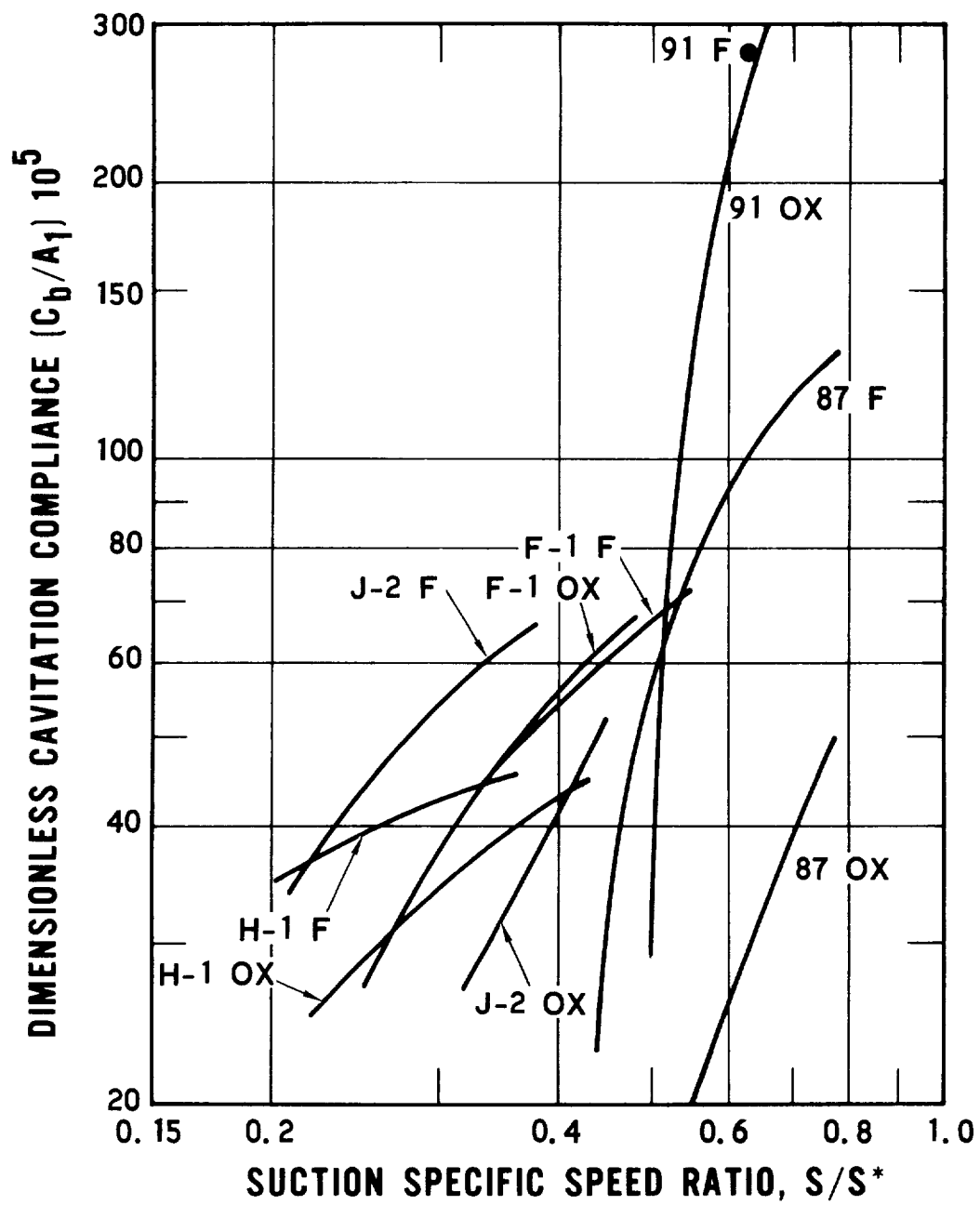


Fig. 9. Dimensionless Pump Cavitation Compliance Versus S/S^*

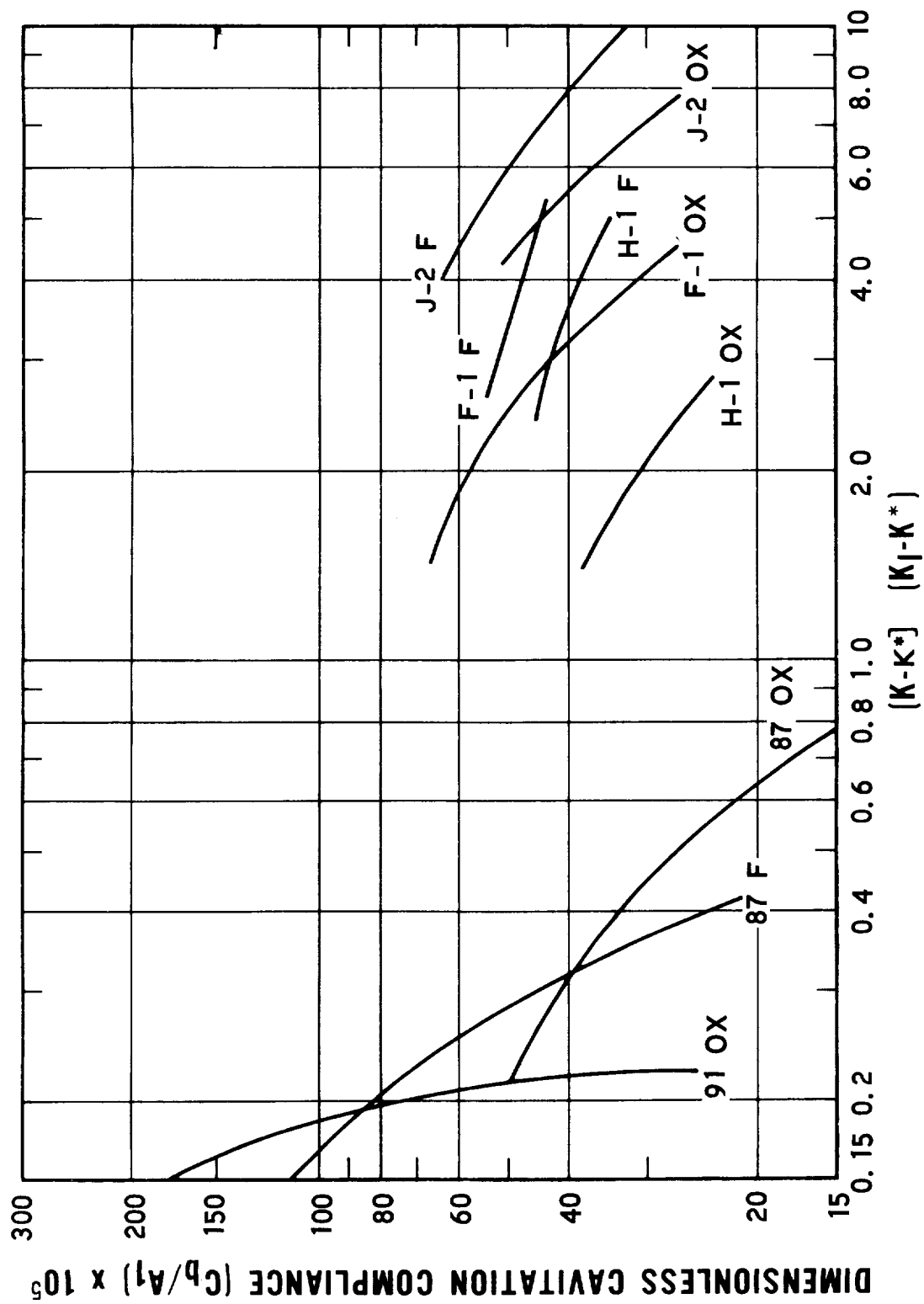


Fig. 10. Dimensionless Pump Cavitation Compliance Versus $(K-K^*) / (K_1-K^*)$

heavy cavitation and that this is true for all the Titan pumps (87 and 91). However, all the Saturn pumps operate above the region where cavitation has a substantial effect on pump performance. While this method of plotting seems to be helpful in correlating the Titan pumps, it is poorer for the Saturn pumps than K/K^* or S/S^* as seen on Figs. 8 and 9, respectively.

For purposes of comparison with the various mathematical models postulated for cavitation compliance in the remainder of this report, the S/S^* plotting of the data on Fig. 9 will be employed. The best of the models are then also compared to the compliance data on the $(K-K^*)/(K_I-K^*)$ basis.

As an aside, it is interesting to note that there is no pattern on Figs. 8 through 10 relative to the TSH effect and pump size, except perhaps for a TSH effect for liquid hydrogen. If in fact these two effects are automatically taken into account by the nondimensionalization, the cavitation compliance data for a nonhydrogen pump can be obtained in advance of full-scale tests by testing a subscale model with water. Then the cavitation compliance of the full-scale pump with propellant can be predicted using a nondimensional form such as that used for Fig. 9, and cavitation performance data for the full-scale pump. The experimental determination of performance of a subscale model using water is a commonly employed tool in pump development, except that propellant is used for a liquid hydrogen pump. The dynamic testing would be merely another form of testing of the same development hardware.

4. MATHEMATICAL MODELS OF PUMP CAVITATION COMPLIANCE

The mathematical models developed for this study are based on empirical prediction of the total volume of cavitation bubbles as a function of the pump operating point. This is followed by a determination of compliance as the product of propellant density and the derivative of the volume with respect to pressure. We will consider three sources of cavitation: (1) cavitation attached to the blades assuming a uniform velocity at the inducer inlet, (2) additional cavitation resulting from the distortion of the velocity distribution at the inducer inlet owing to backflow, and (3) cavitation resulting from the presence of entrained gas in the propellant.

4.1 BUBBLE VOLUME

The general approach to calculating the bubble volume V_b is to establish the bubble cross-sectional area at any radius $A_b(r)$ and then integrate with respect to radius

$$V_b = \int_{r_h}^{r_i} A_b(r) dr \quad (4-1)$$

The free-streamline-wake theory and a number of empirical approaches are considered for calculation of the bubble area and volume.

4.1.1 Bubble Volume from Free-Streamline-Wake Theory

This theory is based on the work by Striping and Acosta (Refs. 5 and 6). They employ a free-streamline-wake theory for a cascade of hydrofoils to calculate the cavity length c and maximum cavity height h for partial cavitation as depicted in Fig. 11. Reference 5 contains the resulting values of h/d and c/d .

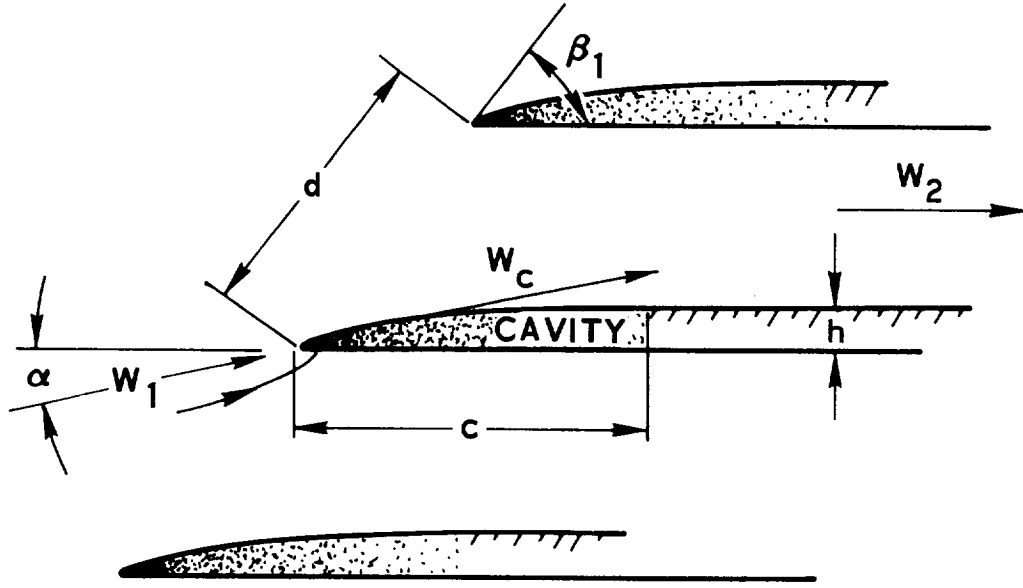


Fig. 11. Sketch of Partly Cavitating Cascade

Appendix A describes the equations and method of approach for calculating the bubble volume and cavitation compliance using the free-streamline-wake theory. The following equation is developed for bubble volume as a function of cavitation number

$$V_b = \frac{8}{3} \pi^2 \sum_{r=r_h}^{r=r_i} \left(\frac{c}{d} \cdot \frac{h}{d} \right) (r^2) \frac{\Delta r}{z} \quad (4-2)$$

where c , h , and d are calculated for each radius and c is a function of cavitation number.

4.1.2 Empirical Approaches to Bubble Volume

The bubble area at any radius is assumed to be related to the bubble area at cavitation breakdown. Figure 12a shows a typical inducer with four blades. In the channel formed by blades A and B, we depict at radius r an area occupied by bubbles at head breakdown $A_b^*(r)/z$. The inlet span (d) is

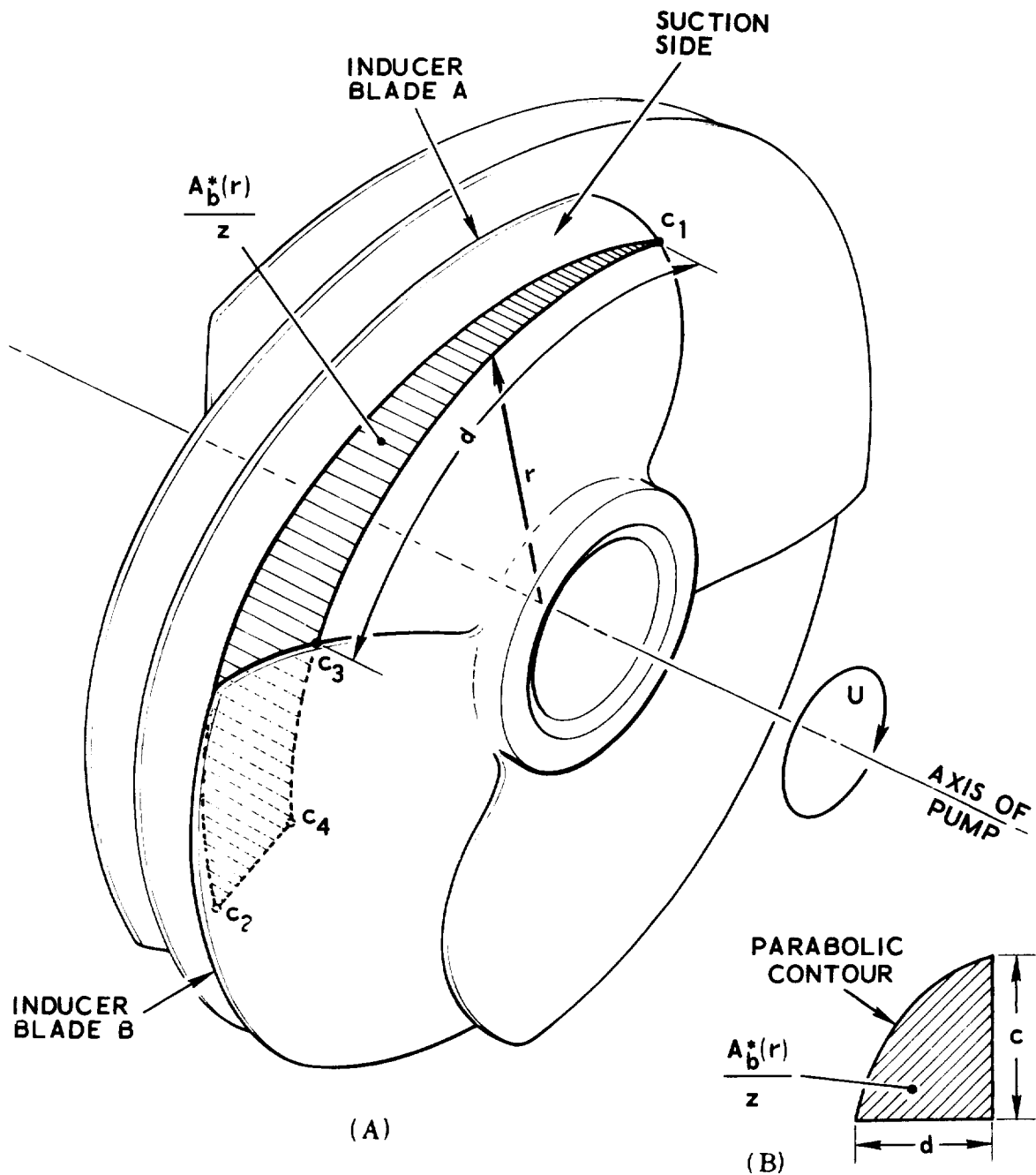


Fig. 12. Bubble Area at Cavitation Breakdown

filled with bubbles and the bubbles fill the channel (shown on the suction side of the blade A between c_1 and c_2 and on the pressure side of blade B between c_3 to c_4 . The shape of the area is quite complex. For simplicity, the actual bubble area between two blades is represented by an equivalent area as shown in Fig. 12b, where d is the span and c is an effective chord length on the suction side of the blade and a parabolic curve forms the third side. Mathematically, the area of bubbles at breakdown, as a function of the radius r , assuming $c = d$ (solidity of one), is then

$$A_b^*(r) = \frac{2}{3} \frac{(2\pi r)^2}{z} \quad (4-3)$$

An alternative assumption is that the chord length of the bubble c_b at breakdown is the product of the stay time of the bubble and the relative velocity

$$c = t W(r)$$

where c = chord length of bubble, t = stay time, and $W(r)$ = relative velocity at pump inlet at any radius. Then

$$A_b^*(r) = \frac{2}{3} (2\pi r) t W(r) \quad (4-4)$$

The stay time t will be determined empirically and $W(r)$ is a function of radius. Next, it is assumed that the area of bubbles at radius r , for a cavitation number above breakdown, is equal to the product of the area of the bubble at breakdown times any of the ratios K^*/K , S/S^* , or $(K_I - K^*)/(K - K^*)$ raised to the exponent n

$$A_b(r) = A_b^*(r) \left(\frac{K^*}{K} \right)^n \quad (4-5)$$

or

$$A_b(r) = A_b^*(r) \left(\frac{S}{S^*} \right)^n \quad (4-6)$$

or

$$A_b(r) = A_b^*(r) \left(\frac{K_I - K^*}{K - K^*} \right)^n \quad (4-7)$$

Either Eq. (4-3) or Eq. (4-4) can be employed for $A_b^*(r)$.

4.2 BLADE CAVITATION COMPLIANCE - MATHEMATICAL MODEL

Our assumption for determining the compliance due to cavitation attached to the blades is that the velocity across the inlet is uniform. All the methods of determining bubble volume described in Section 4.1 are applicable. The free-streamline-wake theory is a theoretical one, based on potential flow theory. This theory can be modified empirically by accounting for the difference between the theoretical cavitation number at breakdown (Ref. 5)

$$K^* \text{ (theory)} = \frac{2 \sin \alpha_i \sin(\beta_i - \alpha_i)}{1 + \cos \beta_i} \quad (4-8)$$

and the value determined by test, as given in Table I. We can then define a modified K for use with the free-streamline-wake theory, called K_{mod} , such that

$$\frac{K_{\text{mod}}}{K} = \frac{K^* \text{ (theory)}}{K^* \text{ (test)}} = K_{\text{ratio}} \quad (4-9)$$

The use of K_{mod} tends to correct for the effects of losses, blade thickness, and TSH effects.

4.3 BACKFLOW CAVITATION COMPLIANCE THEORY - MATHEMATICAL MODEL

4.3.1 General Discussion of Backflow

Backflow in an impeller is defined as the secondary flow that travels in an upstream direction at the impeller inlet. In a previous study (Ref. 2), an empirical method was developed for predicting cavitation compliance for

the unshrouded impellers employed in Titan pumps. In that approach it was assumed that the impeller tip clearance of an unshrouded impeller (radial clearance between the impeller tip and the housing from the inlet eye to the discharge of the impeller) provided a path for backflow and that the degree of backflow is affected by impeller performance. The goal of Ref. 2 was to investigate empirically the importance of the backflow in a cavitation regime using the tip clearance as a path. For the shrouded impeller, however, a different approach is needed. In the following discussion, a theory is proposed for backflow in shrouded and unshrouded impellers.

Backflow takes place as a result of the normal blade-to-blade relative circulation within the impeller channels, as explained in Ref. 7 and depicted in Fig. 13. The fluid moves relative to the blade from the suction side to the pressure side around the discharge side of the impeller (opposite to the direction of rotation). It then travels on the pressure side of the blade towards the inlet (opposite to the direction of through flow), and then turns from the pressure side to the suction side at the inlet (in the direction of rotation). Such a relative circulation can separate at the inlet and travel upstream of the pump. The relative circulation is maintained entirely within the channel if the rate of pressure increase along the blade is small (that is, if the "blade loading" is low). With a high blade loading it becomes possible for the high velocity, high momentum flow traveling along the pressure side to separate before turning to the suction side and then travel upstream of the impeller. In our view, the backflow is an extension of the normal blade-to-blade relative circulation required for the energy transfer from the blade to the fluid. With this concept, backflow could occur in either shrouded or unshrouded impellers at either the eye or hub of the inducer, depending on the condition of blade loading. In general, a design having a high flow coefficient, a high specific speed, a low blade-angle turning rate, and a large number of blades will tend to have low blade loading and, as a result, the backflow will be low.

In addition to backflow caused by channel recirculation, an unshrouded impeller can exhibit a secondary crossflow traveling across the blade tip from the pressure side to the suction side. Depending on the blade loading and on the ratio of tip clearance to the impeller channel span, this crossflow could initiate or amplify a backflow within the impeller channels. In the shrouded impeller, the channel is closed and such crossflow cannot occur.

Backflow and the interaction between backflow and cavitation is evident in the test data of the LR87 fuel pump as presented in Ref. 8. The pump tests were conducted with a series of static pressure taps located circumferentially about the pump inlet and extending about one pump-inlet diameter upstream of the pump. The test data indicated that, at the low suction specific speed values, the pump-inlet pressure was several times higher than the normal pump-inlet pressure, indicating a strong backflow. An example is shown in Fig. 14. As the suction specific speed was increased, the pressure rise was reduced and finally at cavitation levels close to head breakdown the pressure rise at the pump inlet disappeared. This indicates an interaction between cavitation and backflow. Let us assume that the backflow energy traveling upstream with high momentum is independent of the degree of cavitation. Then at low cavitation levels this energy is indicated by a high pressure rise at the pump inlet. As the suction pressure is reduced and cavitation is increased, the backflow momentum retards the bubble forming process, delaying cavitation, and as a result loses part of its strength. Finally, at deep cavitation the backflow momentum is absorbed by the strong cavitation and the inlet pressure is constrained by the vapor pressure. Therefore, a high backflow could lead to a reduction or delay in pump cavitation. This suggests that the strength of the backflow can be measured by the magnitude of the cavitation number at head breakdown.

In support of the foregoing explanation, Ref. 9 shows a comparison between cavitation performance of a shrouded and an unshrouded impeller. The pump is unique, having a high flow coefficient, a low specific speed,

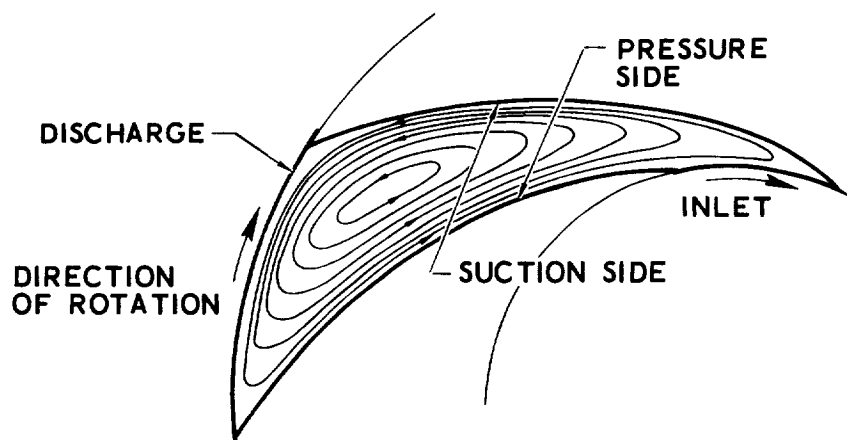


Fig. 13. Relative Circulation Within an Impeller Channel

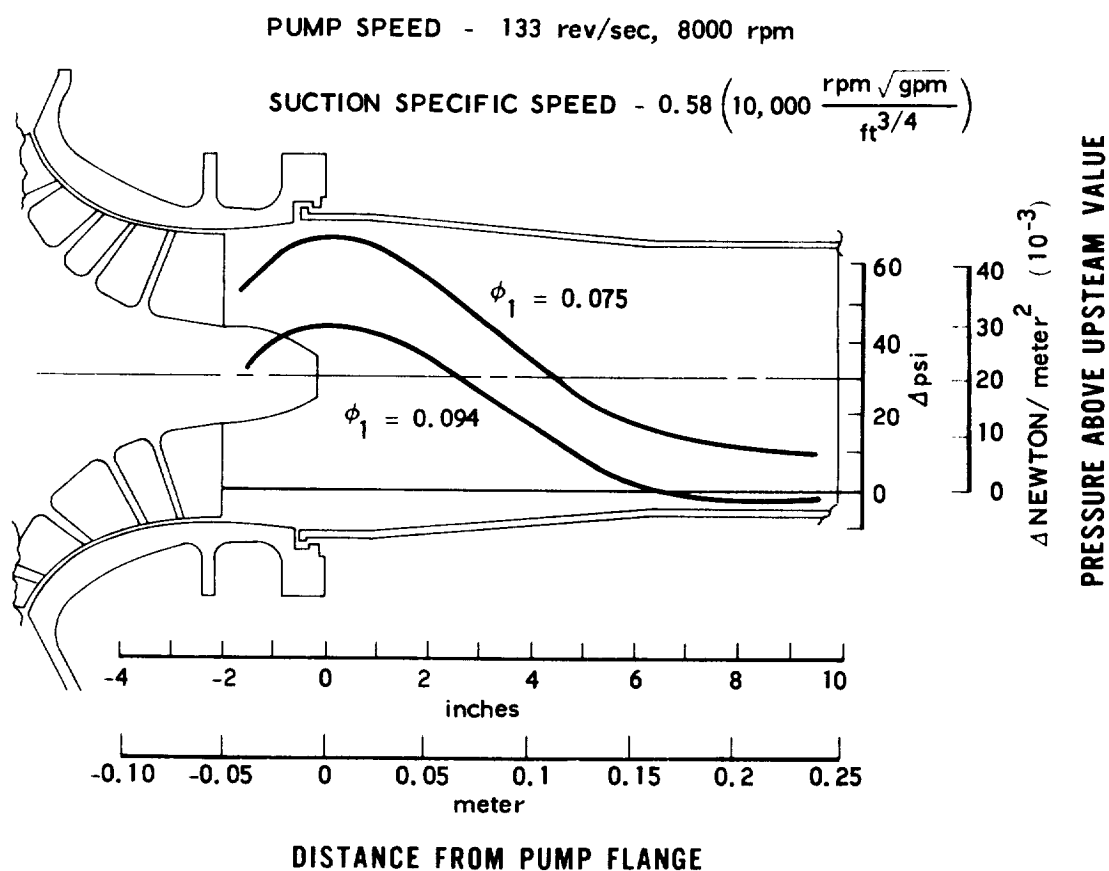


Fig. 14. Indicated Backflow in the LR87 Fuel Pump

and a low ratio of tip clearance to the impeller channel span--all indicating a poor blade loading. This type of pump will have a high backflow whether it is shrouded or not. The test data indicated that the cavitation performance improved (i.e., lower cavitation number at head breakdown) with the unshrouded impeller and improved even more when tip clearance was increased. A similar performance is also reported in Ref. 10 testing several pumps in a wide range of specific speed. These results correlate with the foregoing postulated inhibiting effect of backflow on cavitation.

4.3.2 Pump Performance Related to Backflow

As was discussed in the preceding section, backflow is a function of pump performance. To indicate the relative performance of the pumps under investigation, an attempt is made to calculate performance and design parameters important to backflow. Some of these parameters such as specific speed, efficiency, flow coefficient, cavitation number at breakdown, head coefficient and total head coefficient are already tabulated in Table I. The calculation method for other parameters such as impeller solidity and blade loading are now discussed and the calculated values are summarized in Table II.

The method described in Ref. 5 is used to calculate the solidity τ of an impeller, yielding

$$\tau = \frac{z_{eq} \ln (r_{tm}/r_{lm})}{2 \sin \beta_t} \quad (4-10)$$

where the equivalent number of blades z_{eq} is derived from

$$z_{eq} = \frac{z}{\sin \gamma} \quad (4-11)$$

As shown in Table II, all Titan pumps and the H-1 pumps have solidities of over 2. The new Rocketdyne pumps, F-1 and J-2, have relatively low solidities.

Table II. Pump Performance Prediction Parameters

Parameters	LR87		LR91		F-1		J-2	H-1	
	Fuel	Oxidizer	Fuel	Oxidizer	Fuel	Oxidizer	Oxidizer	Fuel	Oxidizer
Solidity, τ	2.93	2.63	2.46	2.95	1.51	0.925	1.574	3.35	2.17
Diffusion Factor, Δ	0.960	0.928	0.944	0.914	0.770	0.885	0.686	0.876	0.840
Slip Factor, μ	0.865	0.876	0.874	0.86	0.779	0.794	0.772	0.832	0.834
ψ_{Th}	0.772	0.718	0.720	0.757	0.620	0.673	0.586	0.740	0.685
ψ_T	0.874	0.70	0.641	0.840	0.795	0.686	0.664	0.848	0.784
U_1/U_t	0.618	0.754	0.756	0.583	0.686	0.806	0.662	0.517	0.701

The diffusion factor Δ is a measure of blade loading in the impeller. As given in Ref. 11

$$\Delta = 1 - \frac{W_t}{W_1} + \frac{0.75 \psi_{Th}}{(W_1/U_t) \left[\frac{z}{\pi} \left(1 - \frac{U_1}{U_t} \right) + 2 \frac{U_1}{U_t} \right]} \quad (4-12)$$

where ψ_{Th} is the actual Euler head coefficient given by

$$\psi_{Th} = \mu \psi_{\infty} \quad (4-13)$$

The ideal Euler head coefficient ψ_{∞} is

$$\psi_{\infty} = \frac{U_t C_{u_t} - U_1 C_{u_1}}{g} \bigg/ \left(\frac{U_t^2}{g} \right) \quad (4-14)$$

and μ is the slip factor. The slip factor expresses the effect of the deviation of relative flow velocity at the trailing part of the suction side of the blade caused by the relative circulation discussed in Section 4.3.1. An equation developed in Ref. 13 is used for the slip factor

$$\mu = 1 - \frac{2.4 \sin \gamma}{z + 3} \left(1 + \frac{0.833}{z} \right) \quad (4-15)$$

A high value indicates a highly loaded impeller. As shown, all Titan pump blades are highly loaded. Among the Rocketdyne pumps the J-2 oxidizer and F-1 fuel are relatively light in loading, whereas the H-1 pumps and F-1 oxidizer pumps are high in loading.

4.3.3 Pump Performance Prediction

Table II contains the actual Euler head coefficient for the pumps. This head coefficient expresses the torque transmitted from the blade to the fluid. In addition to the Euler head coefficient, there are external losses

such as disc friction, bearing losses, and secondary flow losses which, when added to the Euler head, result in the total head coefficient of the pump. The total head coefficient ψ_T , expressing the torque input to the shaft, is related to the head coefficient ψ and the efficiency η by

$$\psi_T = \frac{\psi}{\eta} \quad (4-16)$$

But, the total head coefficient is the sum of the Euler head coefficient and a term accounting for the external losses

$$\psi_T = \psi_{Th} + \Delta\psi_{Ext} \quad (4-17)$$

Note that if ψ_{Th} is calculated correctly, ψ_T always has a greater value than ψ_{Th} . An important parameter in ψ_{Th} is $U_1 Cu_1/g$, where Cu_1 is the induced prewhirl at the pump inlet. For the values tabulated in Table II, it is assumed that the prewhirl at the pump inlet is zero. There is a possibility that, with a strong backflow, a prewhirl is induced in the direction of rotation at the pump inlet resulting in a lower value of ψ_{Th} than tabulated in Table II. It is also important to note that the ratio of U_1/U_t (or inducer eye to impeller discharge diameter ratio) is an important parameter in determining the significance of the prewhirl component of the Euler head [see Eq. (4-14)]. The higher U_1/U_t , the more effective is the prewhirl contribution. Therefore, the values of U_1/U_t for all the pumps are tabulated in Table II.

4.3.4 Backflow Flow Rate

The backflow flow rate Q_B is a function of the impeller performance parameters that were just discussed. The most important parameters influencing backflow are the impeller diffusion factor Δ , the total head coefficient ψ_T , and the specific speed N_S . The ratio L of backflow flow rate to the incoming flow rate Q_0 is

$$L = \frac{Q_B}{Q_0} = (\text{constant}) \frac{\Delta\psi_T}{N_S} \quad (4-18)$$

The value of the constant is based on the assumption that a good pump will have the following characteristics: $\Delta = 0.6$, $\psi_T = 0.56$ ($\psi = 0.45$ with $\eta = 0.80$), $N_S = 0.093$ (1600 in engineering units), and $L = 0.02$. The result is

$$L = 5.55 \times 10^{-3} \frac{\Delta\psi_T}{N_S} \quad (4-19)$$

4.3.5 Velocity Distribution with Backflow

To determine the velocity distribution at the inducer inlet in the presence of backflow, it is assumed that flow at the tip of the inducer travels upstream. The effect is to reduce the through-flow area. Based on the work presented in Refs. 8 and 12, Fig. 15 indicates the character of the velocity distribution. Three regions of flow are indicated: backflow, transition and a normal constant velocity region. It is assumed that the velocity profiles for both the backflow and transition regions are parabolic and that the radial height of both regions is the same. A detailed analysis of the velocity distribution and other related backflow parameters is given in Appendix B.

4.3.6 Cavitation Compliance with Backflow

The velocity distribution defined in the previous section is used to establish the relative velocity at each radius. For example, see Appendix B for a diagram of the velocity triangle at the tip of the inducer eye. Given the relative velocity, the cavitation number can be determined at each radius. Then any of the three empirical methods for establishing the bubble area $A_b(r)$, as given by Eqs. (4-5) through (4-7), can be applied. Then the total bubble volume is found by integration of the bubble area with respect to radius. This is accomplished for a range of cavitation numbers. Finally, the cavitation compliance is found by differentiating the bubble volume with respect to pressure and multiplying by the fluid density.

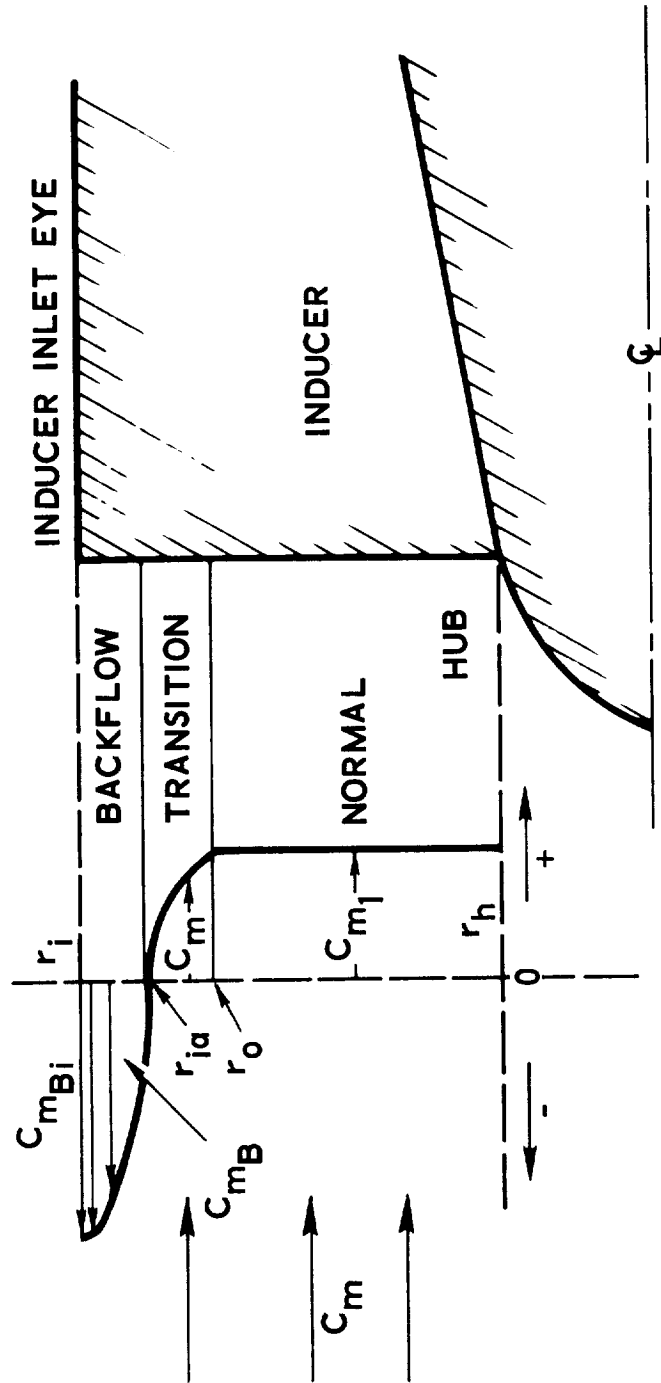


Fig. 15. Assumed Backflow Velocity Distribution at the Inducer Inlet

4.4 GASEOUS CAVITATION - MATHEMATICAL MODEL

Dissolved or entrained gases in the propellants tend to increase the bubble volume and compliance. We shall only consider entrained gases. In Appendix C, a model is developed for the volume of entrained gas within the cavitation region, V_G

$$V_G = \frac{4}{3} \pi^2 (r_i^3 - r_h^3) \frac{RT_S \rho_L}{P_s} X_G \quad (4-20)$$

The total compliance is then the result of the sum of the cavitation and gaseous volumes

$$C_b = - \rho_L \frac{d(V_b + V_G)}{dP_s} \quad (4-21)$$

5. EVALUATION OF MATHEMATICAL MODELS

Results of the mathematical models for blade cavitation and back-flow were compared with the experimental results. Results are first presented for the assumption of a solidity of one for the bubble chord length at breakdown [Eq. (4-3)]. Results for bubble chord length based on stay time [Eq. (4-4)] are then presented for a selected number of the mathematical models. For the gaseous cavitation model no experimental results were available; a sample case for each of the Saturn pumps is presented to show the influence of entrained gas content in the propellant on the compliance.

5.1 FREE-STREAMLINE-WAKE THEORY FOR BLADE CAVITATION COMPLIANCE

As stated in Section 4.2, the Stripling-Acosta free-streamline-wake theory can be used for the mathematical model of blade cavitation compliance. The J-2 fuel pump, being an axial pump, is excluded from the investigation. Figures 16 and 17 present the cavitation compliance for the F-1, H-1 and J-2 pumps (except for the J-2 fuel pump) showing the experimental results and also the predicted values. Figure 16 shows the predicted values without modification of the cavitation number given by Eq. (4-9) (that is, $K_{ratio} = 1$). Figure 17 employs a modified cavitation number, with the values of K_{ratio} presented in Table III. An examination of values of K_{ratio} appearing in Table III shows that for all the pumps, because of the losses and real fluid effects, the values of K_{ratio} are less than one. In addition, because of the TSH effects of the oxidizer, K_{ratio} values for the oxidizer pumps are higher than K_{ratio} for the fuel pumps. Therefore, the use of K_{Mod} seems to provide a logical basis for blade cavitation compliance, since losses and propellant effects are automatically taken into account.

Figure 16 shows that the prediction method using the free-streamline-wake theory yields much lower values than the test results. In the extreme case, the predicted H-1 fuel compliance is two orders of magnitude lower.

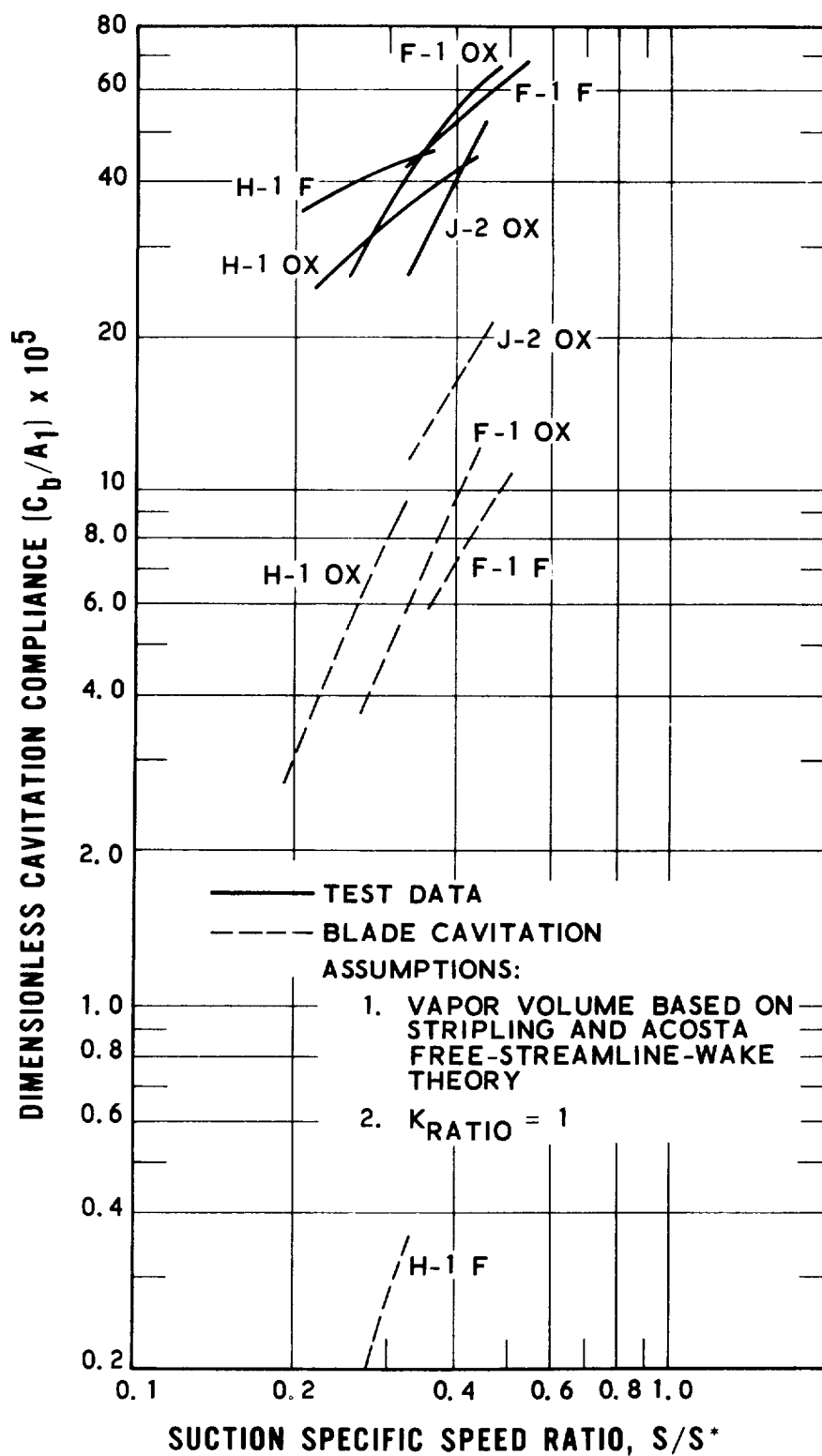


Fig. 16. Test Versus Blade Cavitation Prediction Using Free-Streamline-Wake Theory

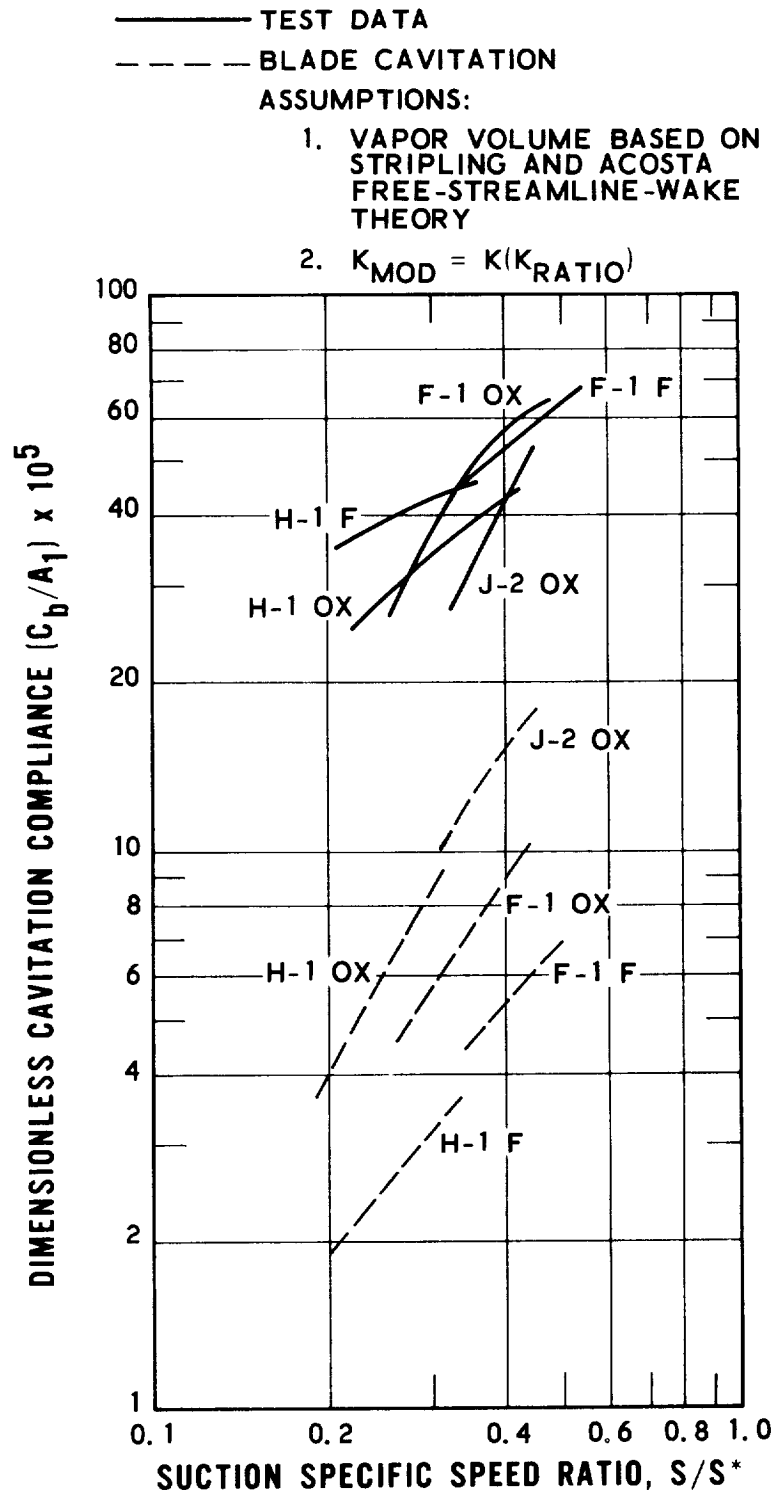


Fig. 17. Test Versus Blade Cavitation Prediction Using Free-Streamline-Wake Theory With K_{Mod}

With use of the K_{Mod} values, the predicted compliances shown in Fig. 17 increase for some of the pumps, but the values are still quite low. We conclude that the free-streamline-wake theory does not apply to the cavitating regimes of rocket pumps. It is probably limited to non-cavitating or incipient cavitation region.

Table III. Values of K_{ratio}

<u>Engine</u>	<u>F-1</u>		<u>J-2</u>		<u>H-1</u>	
Pump	Oxidizer	Fuel	Oxidizer	Oxidizer	Fuel	
K_{ratio}	0.687	0.307	0.795	0.785	0.132	

5.2 RESULTS FOR CAVITATION COMPLIANCE CONSIDERING BACKFLOW

By the method presented in Section 4.3.6, the cavitation compliance considering the effect of backflow on the inlet velocity distribution is calculated for all the Rocketdyne pumps except the J-2 fuel pump. The unity solidity assumption [Eq. (4-3)] is used for these results. In an initial trial, a cavitation number ratio [Eq. (4-5)] with the exponent $n = 1/2$ is used for the backflow region, and the free-streamline-wake theory is used for the transition and normal regions. The computed results are shown in Fig. 18. As can be observed the predicted values are low.

For a next trial, Eq. (4-5) with $n = 1/2$ is used for all three flow regions (backflow, transition and normal). At the same time, to emphasize the effect of incidence angle, a modified value of relative velocity W_1 is used in calculating the cavitation number. It is assumed that, due to free-stream diffusion, the relative velocity at any radius entering the blade is determined as follows:

$$W_1(r) = C_m / \sin \beta \quad (5-1)$$

— TEST DATA
 - - - BLADE CAVITATION

ASSUMPTIONS:

1. THE TRANSITION AND NORMAL SECTIONS VAPOR VOLUME CALCULATION BASE ON THE STRIPLING AND ACOSTA FREE-STREAMLINE-WAKE THEORY WITH K_{MOD}

2. BACKFLOW BUBBLE VOLUME

$$V_b = f(K^*/K)^{1/2} \text{ AND } \tau = 1$$

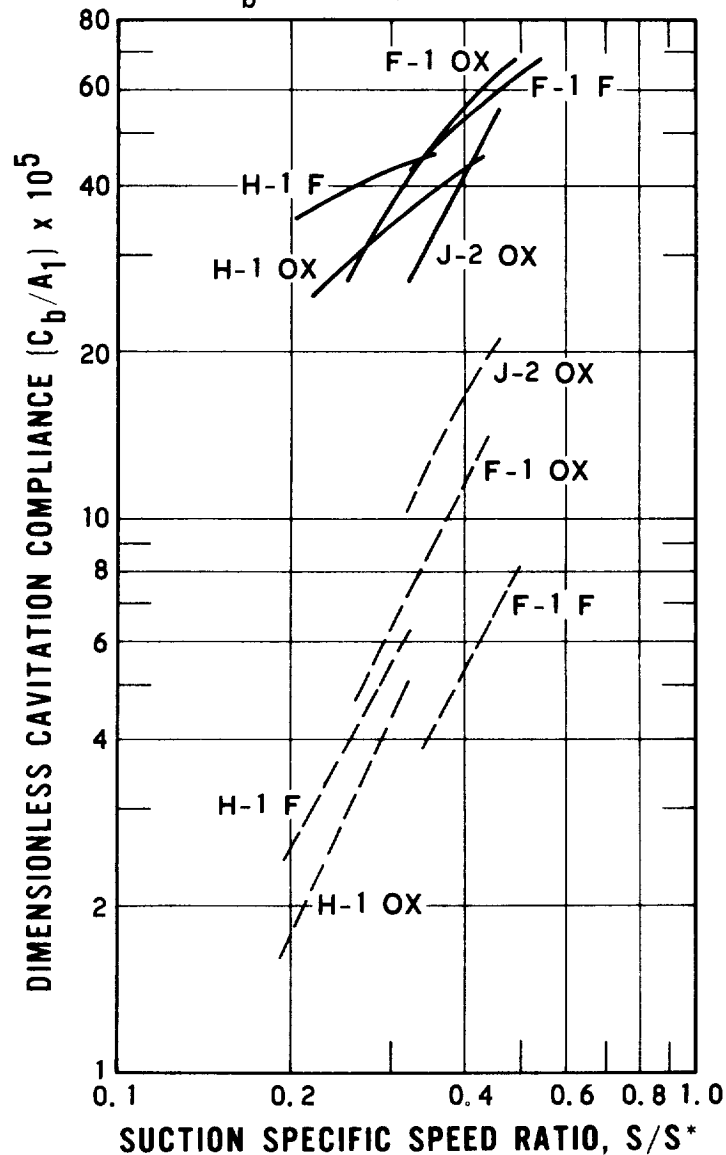


Fig. 18. Test Versus Backflow Cavitation Prediction With $(K^*/K)^{0.5}$ and $\tau = 1$

where β equals the blade angle when the incidence angle $\alpha \leq 4$ deg. For values of $\alpha > 4$ deg, β equals the approach relative velocity angle β_F plus 4 deg. It is further assumed that the shock loss at the inlet is negligible. Recall that W_1 is used in the calculation of K [Eq. (2-1)]. These changes were incorporated in the computer program and the results presented in Fig. 19. As shown, the predictions are now more comparable with the data, although the calculated compliances have higher slopes than do the test results. The calculated compliances for the F-1 pumps cross the test results, the H-1 pumps have low calculated compliances, and the J-2 oxidizer pump has high calculated values. As discussed in Section 2, the J-2 oxidizer pump is expected to have a higher predicted value because of the effect of recirculation to the inducer exit in inhibiting cavitation.

For a third trial the suction specific speed ratio [Eq. (4-6)] is used with $n = 1/2$. In terms of an NPSH ratio, related to the S ratio by Eq. (3-2), the bubble area at any radius is

$$A_b(r) = \frac{8}{3} \frac{\pi^2}{z} r^2 \left(\text{NPSH}^* / \text{NPSH} \right)^{3n/4} \quad (5-2)$$

The results of the compliance calculations are shown in Fig. 20. Comparing Fig. 20 with Fig. 19, some improvement is seen by using the suction specific speed ratio.

To observe the effect of a change of the exponent, n was varied from $1/2$ to 0.15 . The best match was obtained at 0.2 and these results are shown in Fig. 21. The compliances for the J-2 oxidizer pump, the F-1 pumps, and the H-1 oxidizer pump are closer to the test results, but the compliance for H-1 fuel pump is slightly lower than the data presented in Fig. 20.

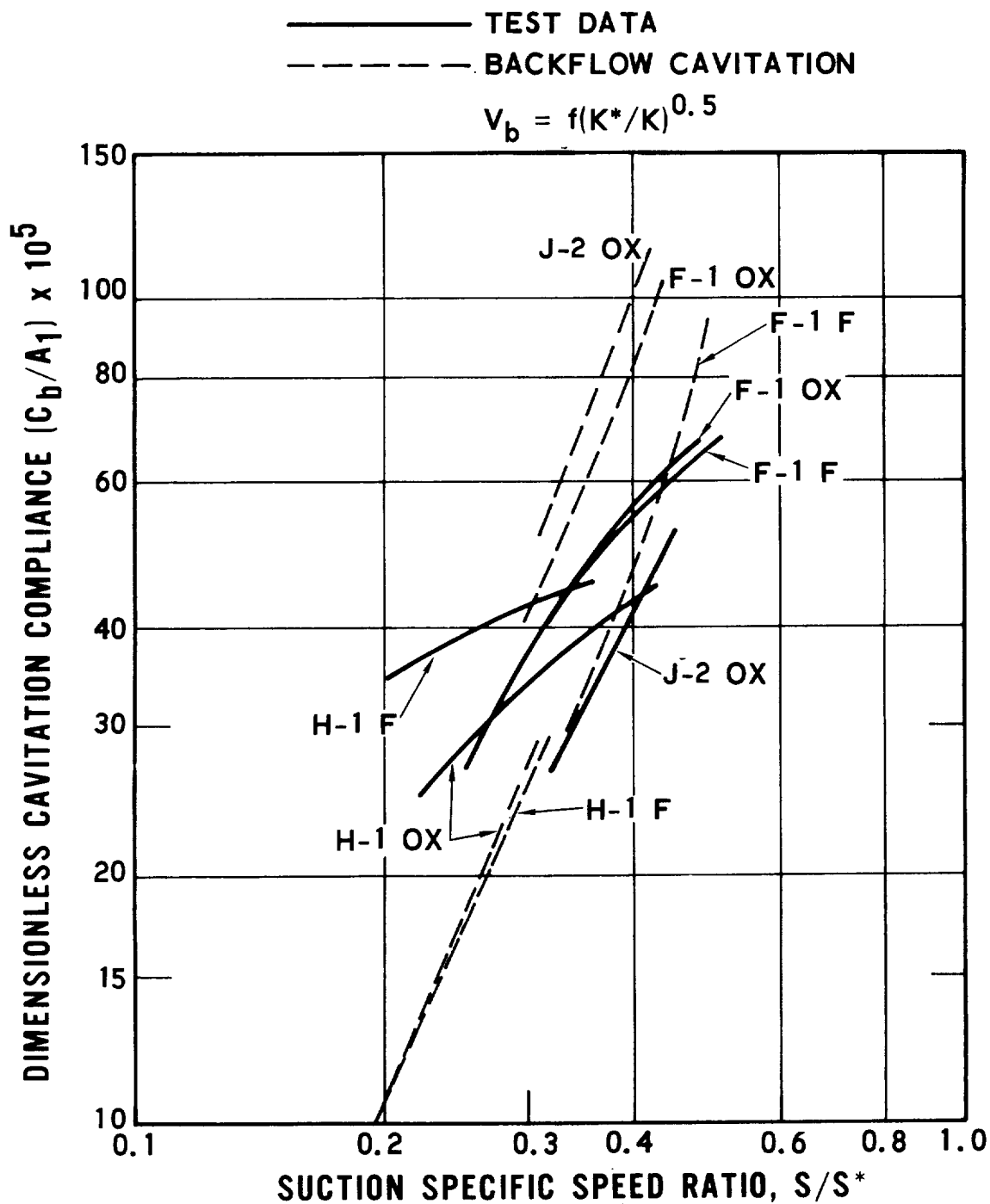


Fig. 19. Test Versus Backflow Cavitation Prediction
With $(K^*/K)^{0.5}$ and $\tau = 1$

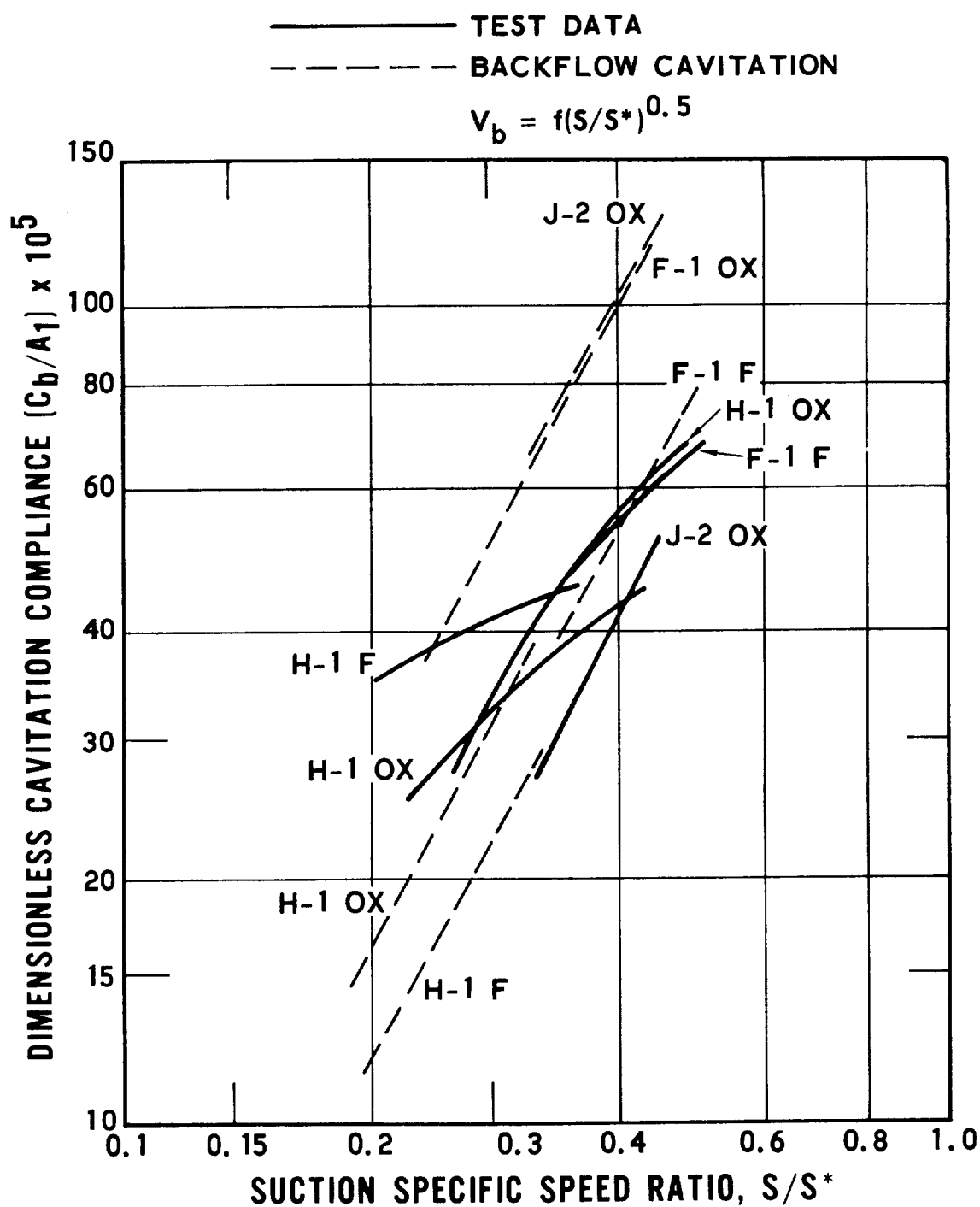


Fig. 20. Test Versus Backflow Cavitation Prediction
With $(S/S^*)^{0.5}$ and $\tau = 1$

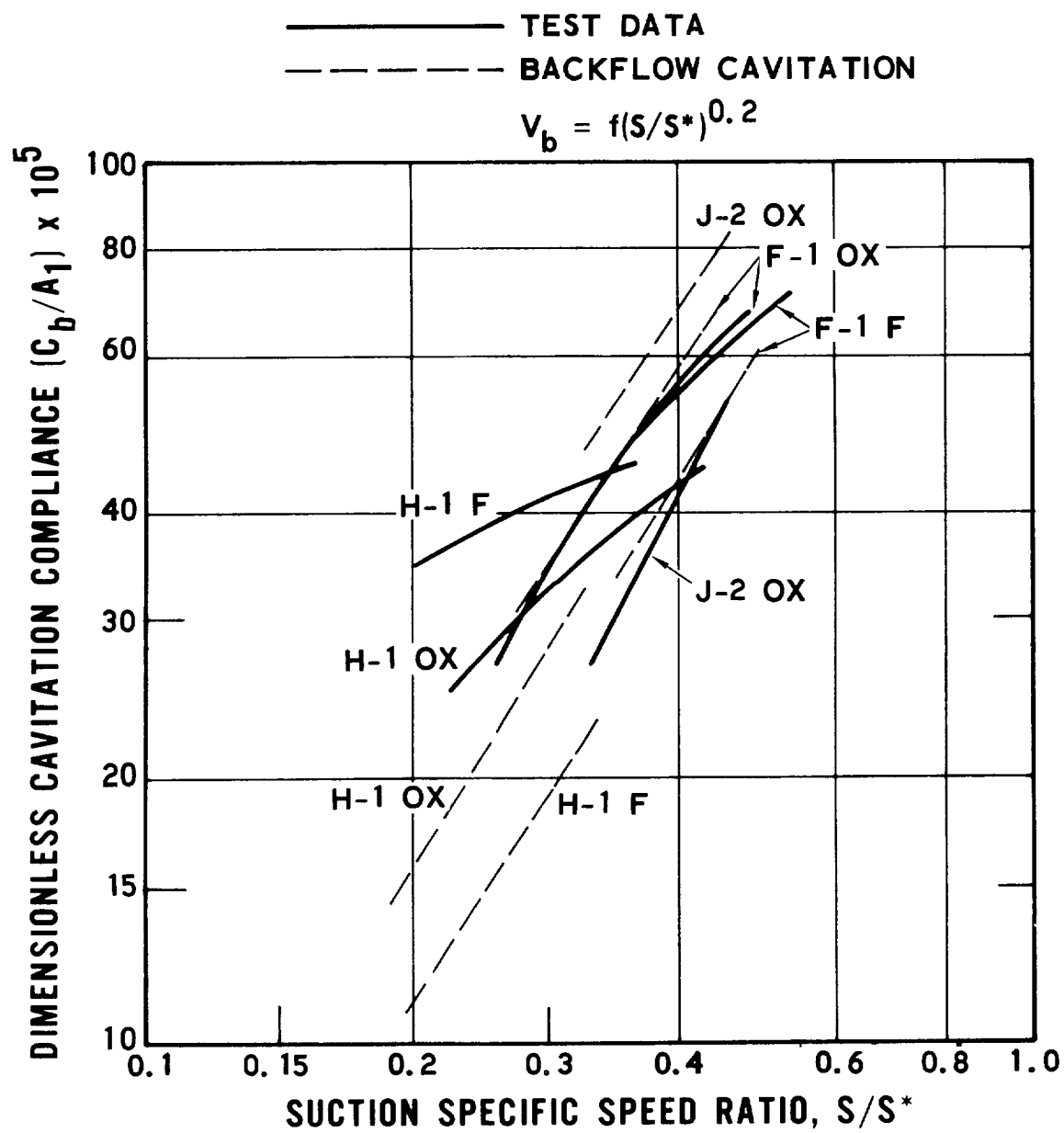


Fig. 21. Test Versus Backflow Cavitation Prediction
 With $(S/S^*)^{0.2}$ and $\tau = 1$

5.3 RESULTS OF EMPIRICAL APPROACHES TO BLADE CAVITATION COMPLIANCE

In the previous section, we accounted for the effect of backflow on the radial distribution of inlet velocity. We considered both the cavitation number ratio and the suction specific speed ratio as a basis for the bubble area at each radius. We took the cavitation number to vary with radius because it depends on relative velocity. However, in our treatment, the suction specific speed ratio is velocity independent and thus is uninfluenced by backflow. For the following reasons we are led to the position that the consideration of backflow is not warranted. First, the use of suction specific speed ratio which is independent of backflow led to as good a correlation with the test data as did the cavitation number ratio, which is dependent on backflow. Second, the consideration of backflow is a significant complication in computations and requires a number of assumptions. Therefore, we now restrict ourselves to the computation of blade cavitation compliance, which implies a uniform velocity at the inducer inlet.

Using S/S^* and unity solidity based [Eqs. (4-3) and (4-6)], we find the bubble volume to be

$$V_b = \frac{8}{9} \frac{\pi^2}{z} (r_i^3 - r_h^3) \left(\frac{NPSH^*}{NPSH} \right)^{3n/4} \quad (5-3)$$

By definition NPSH is related to the static pressure P_s

$$NPSH = \left(\frac{P_s - P_v}{\rho_L} \right) + \frac{C_m^2}{2} \quad (5-4)$$

Assuming $B = P_v/\rho_L - C_m^2/2$

$$NPSH = \frac{P_s}{\rho_L} - B \quad (5-5)$$

Thus Eq. (5-3) becomes

$$V_b = \frac{8}{9} \frac{\pi^2}{z} (r_i^3 - r_h^3) \left(\frac{P_s^*/\rho_L - B}{P_s/\rho_L - B} \right)^{3n/4} \quad (5-6)$$

Taking the derivative with respect to P_s

$$\frac{dV_b}{dP_s} = - \frac{2n\pi^2}{3z\rho_L} (r_i^3 - r_h^3) \left(\frac{P_s^*/\rho_L - B}{P_s/\rho_L - B} \right)^{3n/4} \left(\frac{1}{P_s/\rho_L - B} \right) \quad (5-7)$$

In dimensionless form

$$C_b/A_1 = \frac{2}{3} \frac{n\pi g}{z} \left(\frac{r_i^3 - r_h^3}{r_i^2 - r_h^2} \right) \left(\frac{P_s^*/\rho_L - B}{P_s/\rho_L - B} \right)^{3n/4} \frac{1}{(P_s/\rho_L - B)} \quad (5-8)$$

Using Eq. (5-5)

$$C_b/A_1 = \frac{2}{3} \frac{n\pi g}{z} \left(\frac{r_i^3 - r_h^3}{r_i^2 - r_h^2} \right) \left(\frac{NPSH^*}{NPSH} \right)^{3n/4} \frac{1}{NPSH} \quad (5-9)$$

In engineering units

$$C_b/A_1 = \frac{1}{18} \frac{n\pi}{z} \left(\frac{r_i^3 - r_h^3}{r_i^2 - r_h^2} \right) \left(\frac{NPSH^*}{NPSH} \right)^{3n/4} \frac{1}{NPSH} \quad (5-10)$$

In terms of cavitation number

$$\text{NPSH} = \frac{1}{2} (K_i W_i^2 + C_m^2)$$

and

$$C_b/A_1 = \frac{4}{3} \frac{n\pi g}{z} \left(\frac{r_i^3 - r_h^3}{r_i^2 - r_h^2} \right) \left(\frac{K_i^* W_i^2 + C_m^2}{K_i W_i^2 + C_m^2} \right)^{3n/4} \left(\frac{1}{K_i W_i^2 + C_m^2} \right) \quad (5-11)$$

In engineering units, the only change in Eq. (5-11) is a change of the coefficient from 4/3 to 1/9.

Figure 22 shows the results of calculations for all the pumps (including the J-2 fuel and the Titan pumps) using Eq. (5-9) with $n = 0.2$. Note that the results in Fig. 21 are identical to the corresponding results on Fig. 22. The prediction for the J-2 fuel pump is low compared to the test results. The Titan results except for LR91 fuel show the correct relative position, but have a flatter shape.

If, instead of the unity solidity assumption, we employ the stay time basis for bubble area [Eq. (4-4)], the following equations result:

$$V_b = \frac{4}{3} \pi t \left(\frac{\text{NPSH}^*}{\text{NPSH}} \right)^{3n/4} \sum_{r_h}^{r_i} W_1(r) r \Delta r \quad (5-12)$$

By using Eq. (5-5) to substitute for NPSH

$$V_b = \frac{4}{3} \pi t \left(\frac{P_s^* / \rho_L - B}{P_s / \rho_L - B} \right)^{3n/4} \sum_{r_h}^{r_i} W_1(r) r \Delta r \quad (5-13)$$

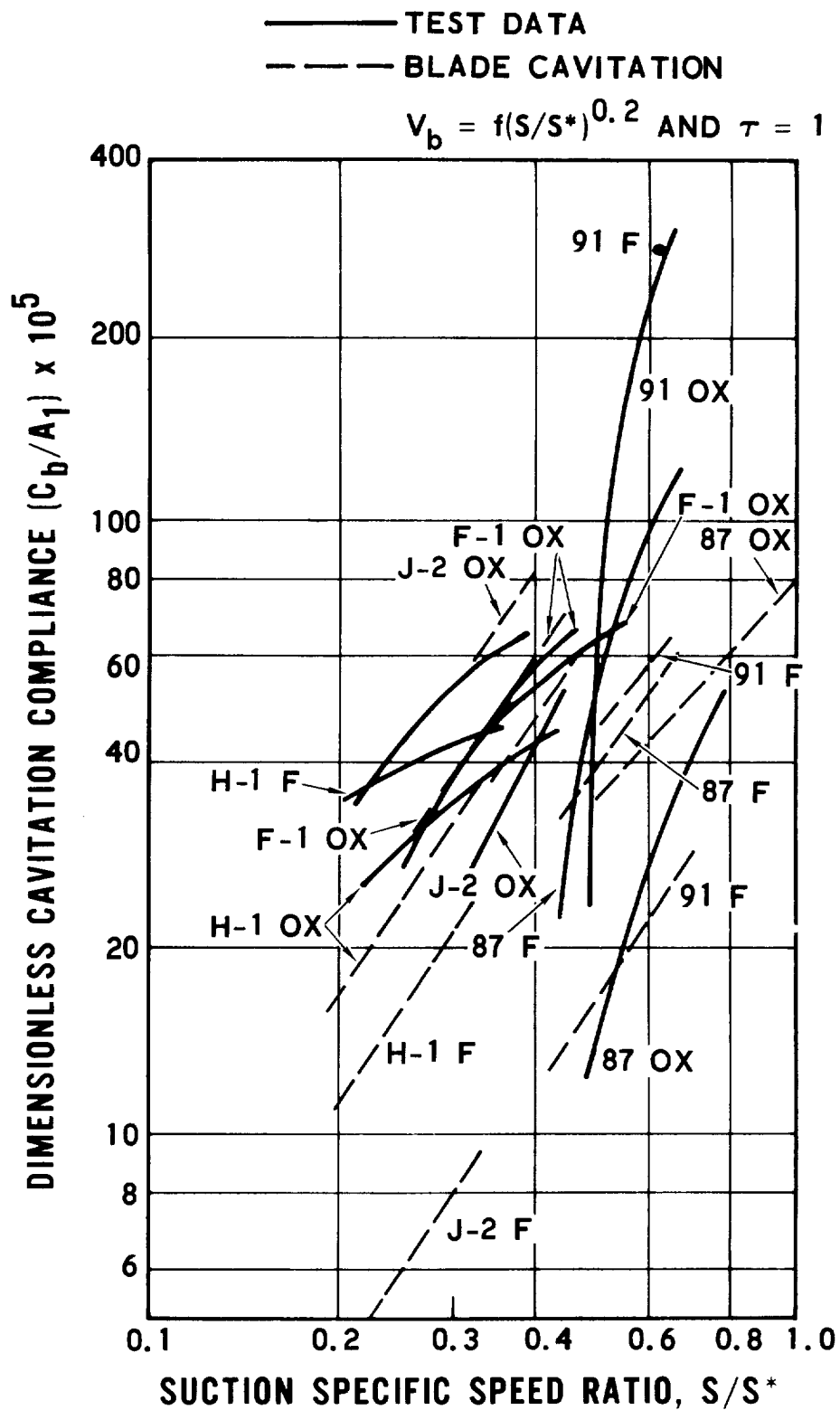


Fig. 22. Test Versus Blade Cavitation Prediction With $(S/S^*)^{0.2}$ and $\tau = 1$

and

$$\frac{dV_b}{dP_s} = - \frac{n\pi t}{\rho_L} \left[\frac{P_s^*/\rho_L - B}{P_s/\rho_L - B} \right]^{3n/4} \left[\frac{1}{P_s/\rho_L - B} \right] \sum_{r_h}^{r_i} W_l(r) r \Delta r \quad (5-14)$$

In dimensionless form

$$C_b/A_1 = \frac{n t g}{(r_i^2 - r_h^2)} \left[\frac{P_s^*/\rho_L - B}{P_s/\rho_L - B} \right]^{3n/4} \left[\frac{1}{P_s/\rho_L - B} \right] \sum_{r_h}^{r_i} W_l(r) r \Delta r \quad (5-15)$$

In terms of NPSH

$$C_b/A_1 = \frac{n t g}{(r_i^2 - r_h^2)} \left(\frac{NPSH^*}{NPSH} \right)^{3n/4} \frac{1}{NPSH} \sum_{r_h}^{r_i} W_l(r) r \Delta r \quad (5-16)$$

In engineering units the coefficient "g" is omitted from Eq. (5-16). Finally, in terms of cavitation number

$$C_b/A_1 = \frac{2 n t g}{(r_i^2 - r_h^2)} \left(\frac{K_i^* W_i^2 + C_m^2}{K_i W_i^2 + C_m^2} \right)^{3n/4} \frac{1}{(K_i W_i^2 - C_m^2)} \sum_{r_h}^{r_i} W_l(r) r \Delta r \quad (5-17)$$

Equation (5-17) is used in the computer program where $W(r)$ is determined for each radius by the method described in Section 5.2 using Eq. (5-1) with free stream diffusion at the inlet of the inducer. It is interesting to note that number of blades, z , does not appear in Eqs. (5-12) through (5-17). Figure 23

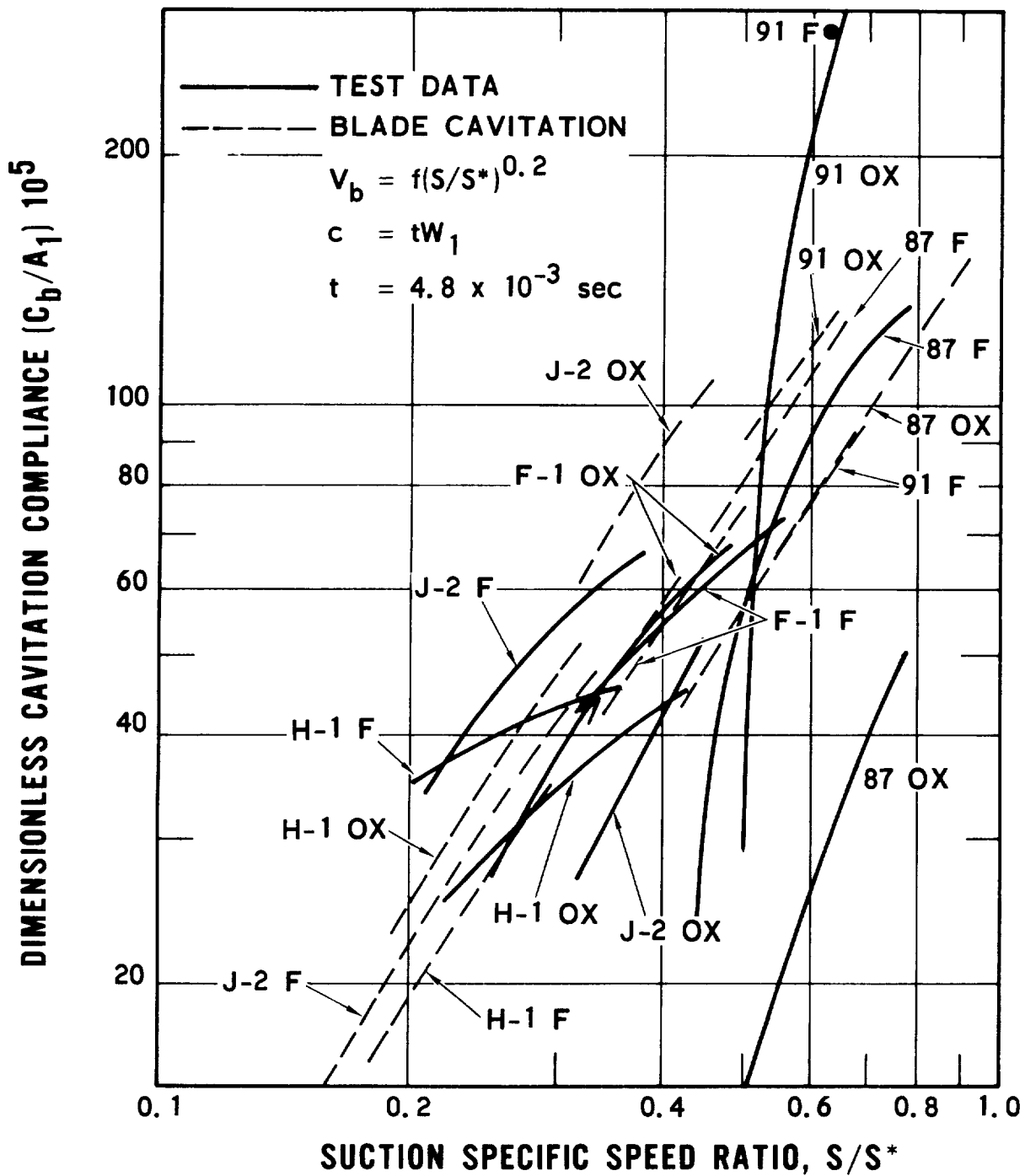
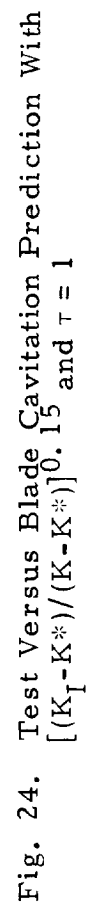


Fig. 23. Test Versus Blade Cavitation Prediction With $(S/S^*)^{0.2}$ and $t = 4.8 \text{ msec}$

shows the results of calculation using Eq. (5-17) with $n = 0.2$ and a value of $t = 4.8$ msec based on an empirical fit of the F-1 oxidizer data. Figure 23 shows reasonable correlation between the test data and prediction for most of the Rocketdyne pumps. For the Titan pumps, although the values for LR87 fuel are close, in general the prediction is poor. The predictions for F-1 pumps are very close and the values for H-1 and J-2 fuel are reasonable. The J-2 oxidizer pump is not predicted well. As pointed out earlier, the recirculatory flow may be inhibiting the cavitation of the J-2 oxidizer pump. All in all, Eq. (5-17) with a single empirically determined value of t appears to yield the best results. Perhaps a further improvement could be realized by accounting for the effect of the heat transfer properties of the propellant on the stay time t , although the propellant heat-transfer difference is not seen between RP-1 and LOX for the F-1 pumps.

Up to this point, all the evaluations were based on presenting the dimensionless cavitation compliance versus S/S^* . We now use Eq. (4-7) to obtain the compliance as a function of $(K_I - K^*)/(K - K^*)$. Both the unity solidity and constant stay time assumptions are used, Eqs. (4-3) and (4-4), respectively.

The results are shown in Fig. 24 for the unity solidity assumption and in Fig. 25 for the constant stay time assumption. In both cases, $n = 0.2$ is assumed. Figure 24 shows that except for H-1 fuel and J-2 fuel the prediction for all Rocketdyne pumps is reasonable. The prediction for the Titan pumps is poor. Figure 25 exhibits the same trend as shown in Fig. 23 for the Rocketdyne pumps, but the values are somewhat closer to the test results. Again, the H-1 fuel and J-2 oxidizer are predicted at low values. However, at low abscissa values the H-1 fuel prediction is close to the test results. For the Titan pumps it is interesting to note that the prediction method shows higher values but the predicted values cross the same way that the test results do. It is postulated that the bubble stay time of 4.8×10^{-3} sec (based on the F-1 oxidizer pump) does not apply to the Titan pumps. The



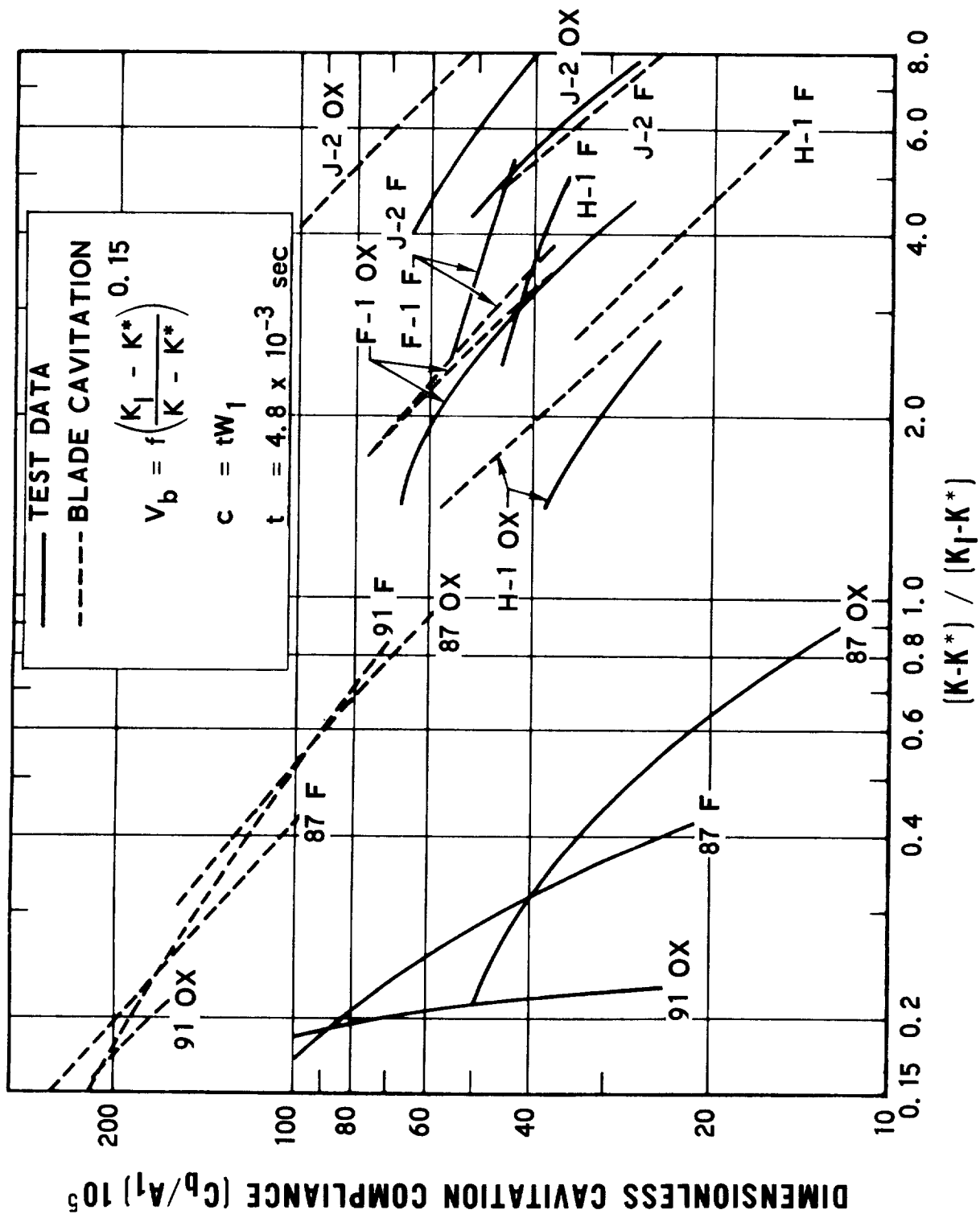


Fig. 25. Test Versus Blade Cavitation Prediction With $[(K_1-K^*)/(K-K^*)]^{0.15}$ and $t = 4.8 \text{ msec}$

Titan inducers are cambered with shorter blade length and the bubble length is expected to be shorter due to the early energy input to the fluid by the blade. For example, if the value of stay time is reduced by 4 times, to 1.2 msec for the Titan pumps, the prediction method will match the test results for LR87 oxidizer and LR87 fuel pumps. The same logic could be used for the J-2 oxidizer pump where the recirculatory flow to the inducer discharge pressurizes the inducer trailing edge and reduces the bubble chord length or stay time. For example, a stay time of 2.4 msec for the J-2 oxidizer pump will match the prediction values with the test results.

5.4 GASEOUS CAVITATION COMPLIANCE

In Section 4.4, an approach was presented for calculating the gaseous cavitation compliance. To demonstrate gaseous cavitation compliance, a sample calculation was made assuming helium gas entrained with a mass fraction X_G of 0.01 percent. The results are shown in Fig. 26 for all the Rocketdyne pumps except the J-2 fuel. As can be observed, the gas content has a significant effect on the cavitation compliance. If one assumes a static pressure of 46 psia and a propellant temperature of 70°F for the F-1 fuel pump, the above gas content corresponds to a 15.5 percent by volume of helium in RP-1.

5.5 CURVE FITTING EQUATION

Although the prediction method provided a reasonable way to calculate the cavitation compliance, it could not be used successfully to predict the compliance for all the pumps. In an attempt to use the data directly, the following curve fit equation was developed to match the Rocketdyne data

$$(C_b/A_1) \times 10^5 = -22.4 + 286 \left(\frac{S}{S^*} \right) - 274 \left(\frac{S}{S^*} \right)^2 + 92.6 \left(\frac{S}{S^*} \right)^3 \quad (5-18)$$

This function is plotted in Fig. 27. In this match of the data, both the J-2 fuel and the J-2 oxidizer pumps are de-emphasized.

Due to poor correlation of data for the Titan pumps, no attempt was made to curve fit the compliance for these pumps.

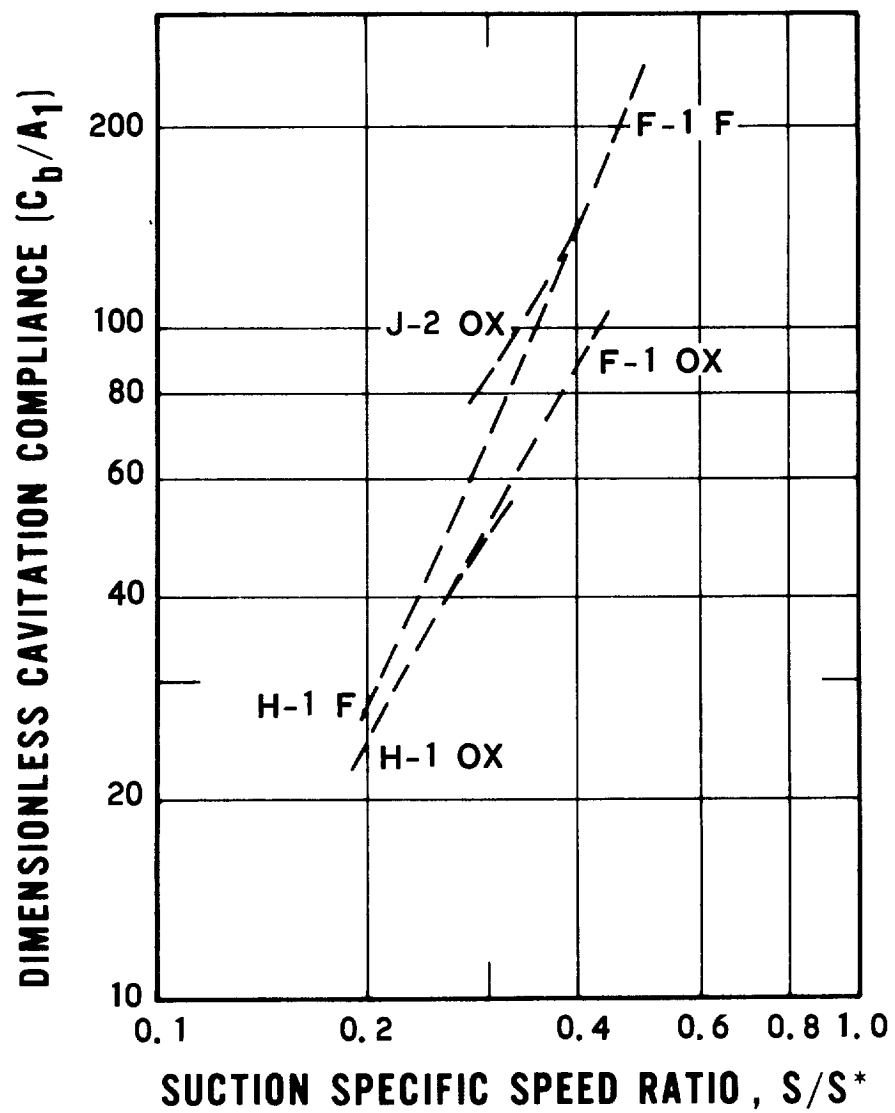


Fig. 26. Predicted Total Compliance With a Gas Content of $X_G = 0.01$ Percent

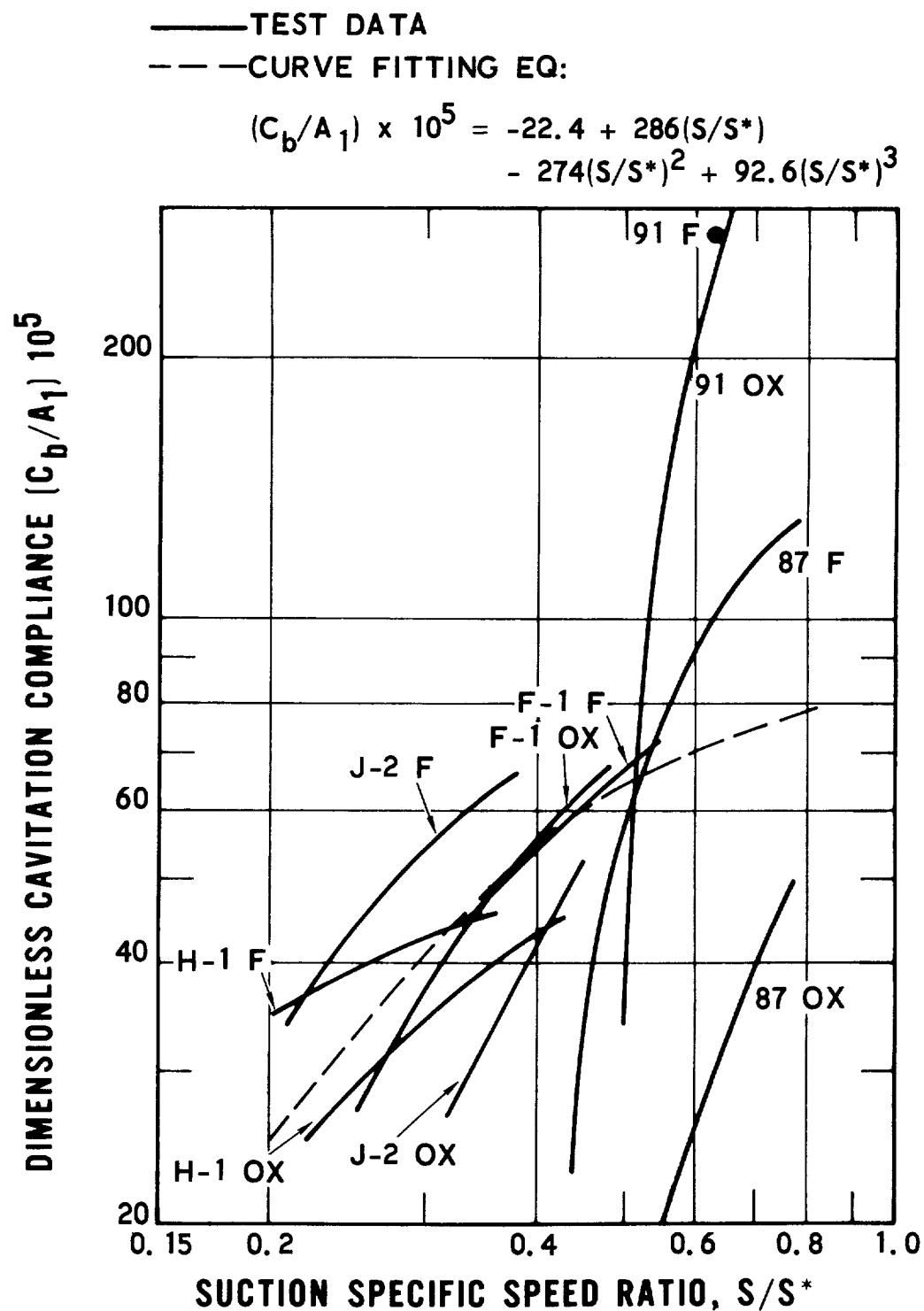


Fig. 27. Comparison Between Test Results and Best Curve Fitting

6. CONCLUSIONS

The following conclusions have resulted from the study of empirical correlation of the cavitation compliance test data and from the studies of mathematical models for predicting cavitation compliance:

(a) The cavitation compliance test data of the H-1 and F-1 Saturn pumps can be correlated quite well by a particular nondimensionalization, as shown in Figs. 8 and 9. This indicates that the influence of pump design, pump size, and propellant properties are inherently taken into account. The nondimensional cavitation compliance is expressed as the volumetric compliance (volume change per unit pressure change) times the propellant weight density, divided by the area of the pump inlet. The nondimensional performance parameter can be any of the following divided by its value at head breakdown: cavitation number, suction specific speed, or net positive suction head. An expression for a best-fit curve is given by Eq. (5-11) and shown in Fig. 27 relative to the test data. The J-2 oxidizer pump is less well correlated because of a unique feature, recirculation to the inducer discharge, which tends to reduce cavitation. The comparison of the J-2 fuel pump with the others is made uncertain because of a lack of accuracy in establishing head breakdown from the available pump performance data.

(b) The above conclusion further suggests that, for the Rocketdyne family of pump designs, the method of empirical correlation can also be employed to relate the cavitation compliance of a subscale pump with water to that of a full-scale pump with propellant. A possible exception is that liquid hydrogen may not have a suitable replacement for this purpose.

(c) The cavitation compliance test data of the LR87 and 91 Titan pumps can be correlated by the nondimensionalization shown in Fig. 10. The nondimensional compliance is the same as that identified in the first conclusion, but the performance parameter is a cavitation-number difference ratio which expresses the relative position of the cavitation number within the range from head breakdown to the point of zero slope of the head rise versus NPSH characteristic.

(d) The blade cavitation compliance predicted by the free-streamline-wake theory is too low, indicating that the assumptions of this theory (potential flow, zero blade thickness) render it inapplicable to the cavitation regime of rocket pumps.

(e) Consideration of the effect of backflow on the velocity distribution across the inducer inlet provides no improvement in the agreement of the mathematical models with test data.

(f) The cavitation compliance of the Saturn H-1 and F-1 pumps can be matched by assuming a bubble proportional to the 0.2 power of the suction specific speed ratio times the bubble volume at head breakdown (see Fig. 23). An equally good alternative is the assumption that the bubble volume is proportional to the 0.15 power of the cavitation-number difference ratio times the bubble volume at head breakdown (see Fig. 25). The volume at breakdown is found by extending the pump inlet area along the inducer blades for a chord length equal to the product of the relative velocity and a stay time empirically determined to be 4.8 msec (see Fig. 23). The use of a chord length corresponding to a solidity of one yields a somewhat poorer correlation; see Fig. 22. On this basis the J-2 oxidizer pump appears to have a shorter stay time, perhaps the result of the recirculation flow's confinement of the bubbles to a shorter distance along the inducer blades.

(g) The cavitation compliance of the Titan pumps can be matched by assuming a bubble volume proportional to the 0.15 power of the cavitation-number difference ratio times the bubble volume at head breakdown; see Fig. 24. The volume at breakdown is like that in conclusion (f), except that the stay time is approximately 1.2 msec. A shorter stay time relative to the Rocketdyne pumps is to be expected because of the cambered design of the inducer blades of the Titan pumps.

(h) A method has been formulated for predicting the contribution of entrained gas to cavitation compliance. No data are available for evaluation of the method.

7. RECOMMENDATIONS

The following recommendations are made for prediction of cavitation compliance for new pump designs in the Rocketdyne family:

(a) Prior to the availability of experimental data on a subscale or fullscale pump, it is recommended that two methods be employed to estimate the nondimensional cavitation compliance. They are:

1. The best-fit curve of Eq. (5-18) shown in Fig. 27, and
2. The mathematical model which assumes a bubble volume proportional to the 0.2 power of the suction specific speed ratio times the bubble volume at head breakdown, along with a stay time of 4.8 msec, as exemplified in Fig. 23.

Any difference between the two estimates is an indication of their uncertainty. The cavitation compliance can then be estimated using the predicted position of head breakdown.

(b) If subscale pumps are evaluated during the development of the new design, pulsing tests should be performed to establish a nondimensional plot of cavitation compliance such as that of Figs. 8 or 9. Particular attention should be paid to establishing the position of head breakdown during the performance testing. The cavitation compliance of the fullscale pump is predicted by assuming it possesses the identical nondimensional cavitation compliance characteristic, even if water has been substituted for the propellant for the subscale tests.

(c) It is recommended that the cavitation compliance of subscale models of the existing Rocketdyne pumps be determined experimentally to obtain an additional basis for empirical correlation.

APPENDIX A
BLADE CAVITATION COMPLIANCE

In Ref. 5, the free-streamline-wake theory is used to calculate the cavity height and length at an inducer leading edge radius

$$h/d = \sin\beta \left[1 - R \frac{\sin(\beta - \alpha)}{\sin\beta} \right] \quad (A-1)$$

$$\begin{aligned} c/d = \frac{1}{2\pi} & \left\{ 2\pi \sin(\beta - \alpha) \left[R + \frac{1}{R(K+1)} \right] \ln \left[\frac{R\sqrt{K+1} + 1}{R\sqrt{K+1} - 1} \right] \right. \\ & - \left[\sin\beta + \left(\frac{1}{K+1} \right) \sin(\beta - 2\alpha) \right] \ln \left[\frac{(\sqrt{K+1} + \cos\alpha)^2 + \sin^2\alpha}{(\sqrt{K+1} - \cos\alpha)^2 + \sin^2\alpha} \right] \\ & \left. + 2 \left[\cos\beta + \left(\frac{1}{K+1} \right) \cos(\beta - 2\alpha) \right] \tan^{-1} \left(\frac{2\sqrt{K+1} \sin\alpha}{K} \right) \right\} \quad (A-2) \end{aligned}$$

where

$$R = w_1/w_2$$

$$\alpha = \beta - \beta_F$$

$$d = \text{blade spacing}$$

From Ref. 4, w_2 is given by the following equation

$$w_c/w_2 + w_2/w_c = \left(\frac{w_c}{w_1} + \frac{w_1}{w_c} \right) \cos\alpha + \left(\frac{w_c}{w_1} - \frac{w_1}{w_c} \right) \sin\alpha \tan(\gamma + \alpha) \quad (A-3)$$

where

$$w_c = w_1 \sqrt{1 + K} \quad (A-4)$$

In using these equations it is assumed that

$$\beta = f(r)$$

In most cases, the leading edge is a radial element or has a constant pitch. For the radial element blades

$$r \tan \beta = \text{Constant} \quad (A-5)$$

Another important parameter is the axial velocity (C_{m1}) flow coefficient (ϕ_1) distribution at the leading edge as a function of radius.

$$\phi_1 = \frac{C_{m1}}{U_i} \quad (A-6)$$

It is assumed that ϕ_1 is constant along the leading edge of the reducer.

For the initial estimation it was also assumed that the blade thickness was zero, and axial velocity and pressure distribution at the inlet were uniform. With these assumptions in mind, the inducer blade radii from eye to the hub were divided into several stations and the cavity height and lengths were determined for each station. By using the cross-sectional area of the cavity and the radius increment (Δr) between the radial stations, the bubble volume was then determined. The following equations were used.

Main inputs are

$$K_i, r_i, U_i, \text{ and } \phi_1$$

By definition the local cavitation number at any radius is

$$K_j = \frac{NPSH - \frac{C_m^2}{2}}{W_j^2/2} \quad (A-7)$$

NPSH and C_m are constant at the inlet but W_j varies with radius and assuming no prewhirl at the inlet

$$W_j^2 = U_j^2 + C_m^2 \quad (A-8)$$

Equation (A-7) can be written in the following form

$$K_j = \frac{\frac{2NPSH}{U_i^2} - \phi_1^2}{\frac{U_j^2}{U_i^2} + \phi_1^2} \quad (A-9)$$

and

$$K_i = \frac{\frac{2NPSH}{U_i^2} - \phi_1^2}{1 + \phi_1^2} \quad (A-10)$$

Therefore, K_j can be described in terms of K_i

$$K_j = \frac{K_i (1 + \phi_1^2)}{\frac{U_j^2}{U_i^2} + \phi_1^2} \quad (\text{A-11})$$

but

$$\frac{U_j}{U_i} = \left(\frac{r_j}{r_i} \right) \quad (\text{A-12})$$

Therefore

$$K_j = \frac{K_i (1 + \phi_1^2)}{\left(\frac{r_j}{r_i} \right)^2 + \phi_1^2} \quad (\text{A-13})$$

With the assumption of no prewhirl the relative angle of flow at any radius is

$$\tan \beta_{f_j} = C_m / U_j \quad (\text{A-14})$$

using Eq. (A-12)

$$\tan \beta_{f_j} = \frac{C_m}{U_i \frac{r_j}{r_i}}$$

or

$$\tan \beta_{f_j} = \phi_1 \frac{r_j}{r_i} \quad (\text{A-15})$$

The incidence angle

$$\alpha_j = \beta_j - \beta_{f_j} \quad (\text{A-16})$$

With the above information the values of c/d and h/d at any radius can be determined. The area of the cavity, for each blade, at any radius, assuming parabolic cavity shape is given by

$$A_c = \frac{2}{3} \left(\frac{c}{d} \cdot \frac{h}{d} \right) d^2 \quad (\text{A-17})$$

$$d = \frac{2\pi r}{z}$$

$$A_c = \frac{8\pi^2}{3} \left(\frac{c_j}{d} \cdot \frac{h_j}{d} \right) \left(\frac{r_j}{z} \right)^2$$

The cavity volume along the radius for all blades

$$V = \frac{8}{3} \pi^2 \sum_{r_j=r_h}^{r_j=r_i} \left(\frac{c_j}{d} \cdot \frac{h_j}{d} \right) (r_j^2) \frac{\Delta r}{z} \quad (\text{A-18})$$

To obtain $-dV/dP_s$ values, using cavitation number equation

$$P_s = \frac{W_i^2 K_i \rho_L}{2} + P_v \quad (\text{A-19})$$

The value of dV/dP is obtained graphically by plotting V versus P_s . Finally, the dimensionless cavitation compliance $C_b/A_1 = (-dV/dP) \rho_L/A_1$.

APPENDIX B

BACKFLOW CAVITATION COMPLIANCE

Figure 14 shows the assumed velocity profile for a pump with backflow and the profile is divided into three regions:

1. Backflow region
2. Transition region
3. Normal region

In the following discussion the velocity distribution and the related values required for the calculation of c/d and h/d using the free-streamline-wake theory are calculated.

I. BACKFLOW REGION

It is assumed that the backflow Euler head at the eye of inducer equals half of the power head generated by the pump

$$U_B C_{u_B} / g = \frac{\psi_T U_t^2}{2g} \quad (B-1)$$

where U_B and C_{u_B} are determined for each radius and blade angle.

Assuming that backflow follows the blade, the velocity triangle for the backflow is shown in Fig. 28. In Fig. 28, C_L is the absolute velocity of the backflow, W_B is the relative velocity and U_B the tangential velocity. C_{m_B} is the meridional or axial component of absolute velocity.

$$C_{m_B} = C_L \sin \theta_B \quad (B-2)$$

and from the velocity triangle

$$C_L \sin \theta_B = W_B \sin \beta_B \quad (B-3)$$

$$C_L \cos \theta_B = U_B + W_B \cos \beta_B \quad (B-4)$$

Knowing C_L and β_B the values of θ_B and W_B can be determined.

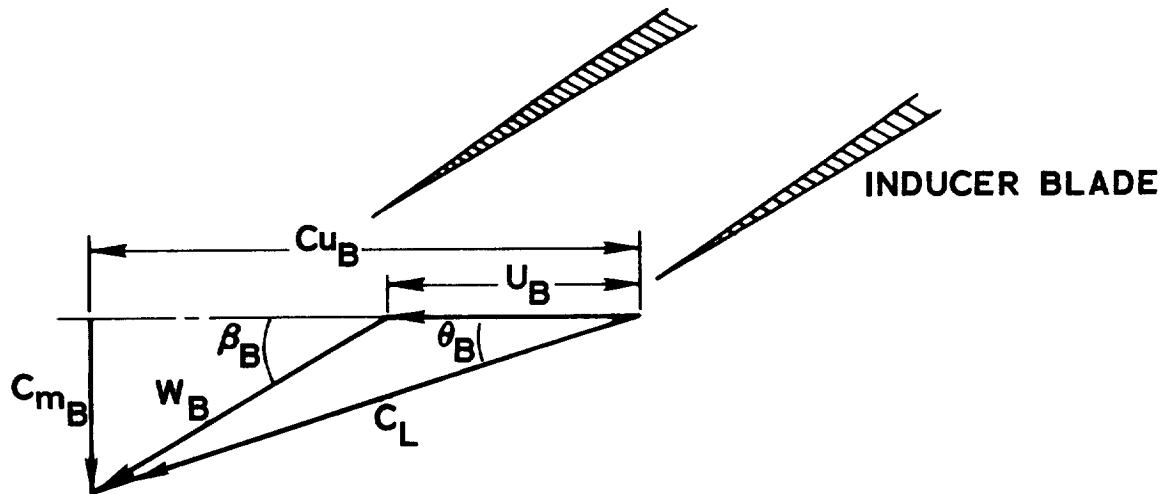


Fig. 28. Velocity Triangle for the Backflow Region

It is assumed that C_m distribution is parabolic along the radius with the maximum C_m at the outer diameter and zero value at the minimum diameter as shown in Fig. 15. Thus

$$C_{mB}^2 = \frac{C_{mBi}^2}{(r_i - r_{ia})} (r - r_{ia}) \quad (B-5)$$

where C_{m_B} corresponds to the velocity at r . Knowing the value of $C_{m_{Bi}}$, to determine the value of r_{ia} the following integration is used:

$$Q_B = \int_{r_{ia}}^{r_i} \frac{C_{m_{Bi}}}{(r_i - r_{ia})^{1/2}} (r - r_{ia})^{1/2} (2\pi r) dr \quad (B-6)$$

and

$$Q_B = \frac{4\pi}{15} C_{m_{Bi}} (3r_i - 2r_{ia}) (r_i - r_{ia}) \quad (B-7)$$

At this point, the region of backflow extends from r_{ia} to r_i . And at every r the value of C_{m_B} , β , U , W are known. Assuming the flow follows the blade, $\alpha = 0$ and $\beta = \beta_F$. It is also assumed that the static pressure at the backflow region equals stagnation pressure at the normal region of the pump. Therefore

$$P_{sB} = P_s + \frac{C_m^2 \rho_L}{2} \quad (B-8)$$

where P_s and C_m refer to static pressure and axial component of velocity "normal region" which will be considered later.

$$K_B = \frac{(P_{sB} - P_V)}{\rho_L W_B^2 / 2} \quad (B-9)$$

The only variable in the above equation is W_B which is a function of radius, and is obtained from the velocity triangle $W_B = C_{m_B} / \sin \beta$.

At this point the input values are known and the empirical equations presented in the text are used to calculate compliance.

II. TRANSITION AND NORMAL REGIONS

As shown in Fig. 15, these two regions constitute the through flow velocity profile. The transition region extends a radial length equal to the radial length of the backflow region.

$$r_{ia} - r_o = r_i - r_{ia} \quad (B-10)$$

and has parabolic velocity distribution. At the upper radius the value of velocity is zero and at the lower radius the velocity equals C_{m1} (the through velocity for the normal region). So

$$C_{mTrans.}^2 = \frac{C_{m1}^2}{(r_{ia} - r_o)} (r_{ia} - r) \quad (B-11)$$

and

$$\phi_{1Trans.} = \frac{C_{mTrans.}}{U_i} \quad (B-12)$$

In the "normal region" C_{m1} is constant and

$$\phi_1 = \frac{C_{m1}}{U_i} \quad (B-13)$$

To determine C_{m1}

$$Q_{Trans.} + Q_N = Q_o \quad (B-14)$$

$$Q_{Trans.} = \frac{4\pi}{15} C_{m1} (2r_{ia} + 3r_o) (r_{ia} - r_o) \quad (B-15)$$

$$Q_N = \pi C_{m1} (r_o^2 - r_h^2) \quad (B-16)$$

Combining Eqs. (B-14), (B-15) and (B-16)

$$C_{m1} = \frac{Q_o}{\frac{4\pi}{15} (2r_{ia} + 3r_o)(r_{ia} - r_o) + \pi(r_o^2 - r_h^2)} \quad (B-17)$$

and

$$C_{mTrans.} = \frac{Q_o (r_{ia} - r)^{1/2}}{(r_{ia} - r_o)^{1/2} \left[\frac{4\pi}{15} (2r_{ia} + 3r_o)(r_{ia} - r_o) + \pi(r_o^2 - r_h^2) \right]} \quad (B-18)$$

Therefore, the C_m distribution is known and using the method explained in Appendix A the values of $V_{Trans.} + N$ are determined for a radius range of r_{ia} to r_h .

The total vapor volume for a pump with backflow is

$$V = V_{Trans.} + N + V_B \quad (B-19)$$

and $-dV/dP_s$ is determined graphically. Finally, $C_b = -dV/dP (\rho_L)$.

APPENDIX C

GASEOUS CAVITATION COMPLIANCE

It is assumed that gas is entrained in the propellant and the propellant flow is a mixture of gas and liquid. The gas properties and the mass fraction of gas in liquid are known. It is also assumed that the gas volume change follows perfect gas laws and the process is isothermal. It is also assumed that X_G , the mass fraction of gas in liquid, is known

$$X_G \doteq M_G/M_L \quad (C-1)$$

Then

$$X_G = \frac{V_G}{V_L} \frac{\rho_G}{\rho_L} \quad (C-2)$$

but

$$\rho_G = \frac{P_s}{RT_s}$$

and

$$\frac{V_G}{V_L} = X_G \frac{RT_s \rho_L}{P_s} \quad (C-3)$$

Assuming that up to a solidity of one the static pressure is basically equal to the suction pressure but beyond that the pressure increases and the gas volume becomes insignificant. At any radius

$$\Delta V_L = (2\pi r)^2 \frac{\Delta r}{z} \quad (C-4)$$

using Eq. (C-3) and substituting ΔV_L for V_L and ΔV_G for V_G

$$\Delta V_G = 4 \frac{\pi r^2}{z} \frac{RT_s \rho_L}{P_s} X_G (\Delta r) \quad (C-5)$$

Integrating with respect to radius

$$V_G = \int_{r_h}^{r_i} 4 \frac{\pi r^2}{z} \frac{RT_s \rho_L}{P_s} X_G dr \quad (C-6)$$

and

$$V_G = \frac{4}{3} \pi^2 (r_i^3 - r_h^3) \frac{RT_s \rho_L}{P_s} X_G \quad (C-7)$$

Then total cavitation compliance

$$C_b/A = - \frac{d(V_b + V_G)}{dP_s} \frac{\rho_L g}{A_1} \quad (C-8)$$

REFERENCES

1. Anon., "Prevention of Coupled Structure - Propulsion Instability (POGO)," NASA Space Vehicle Design Criteria (Structures) SP-8055 (1971).
2. Ghahremani, F. G., "Turbopump Cavitation Compliance," The Aerospace Corporation, Report No. TOR-0059(6531-01)-2 (September 1970).
3. Vaage, R. D., L. E. Fidler, and R. A. Zehnle, "Investigation of Characteristics of Feed System Instability," Report MCR-72-107, Martin Marietta Corp. (May 1972).
4. "Titan B/C/D Standard Space Launch Vehicle Development Report for the MMC Prevalve Test Evaluation," Report 9111-A-085-2, Aerojet Liquid Rocket Company (April 1970).
5. Stripling, L. B. and A. J. Acosta, "Cavitation in Turbopumps - Part I," Journal of Basic Engineering, Transactions of the ASME (September 1962).
6. Stripling, L. B., "Cavitation in Turbopumps - Part 2," Journal of Basic Engineering, Transactions of the ASME (September 1962).
7. Stepanoff, A. J., Centrifugal and Axial Flow Pumps, 2nd Ed., John Wiley and Sons, Inc., New York (1957).
8. Norquist, L. W. S., et al, "Development of Close-Coupled Accumulators for Suppressing Missile Longitudinal Oscillations (POGO)," AIAA Paper No. 69-547, American Institute of Aeronautics and Astronautics, New York (June 1969).
9. Miller, M. J., et al, "Detailed Performance of a Radial-Bladed Centrifugal Pump Impeller in Water," NASA Tn D-4613, Lewis Research Center (June 1968).
10. Wood, G. M., et al, "Tip-Clearance Effects in Centrifugal Pumps," ASME Paper 64-WA/FE-17, ASME, New York.
11. Coppage, J. E., et al, "Study of Supersonic Radial Compressors for Refrigeration and Pressurization System," WADC Technical Report 55-2571 (February 1956).

REFERENCES (Continued)

12. Badowski, H. R., "An Explanation of Instability of Cavitating Inducers," ASME Cavitation Forum (1969).
13. Sakai, Toshimichi, et al, "On the Slip Factor of Centrifugal and Mixed-Flow Impellers," ASME Paper 67-WA/GT-10, Pittsburg, Pa. (November 1967).

INTERNAL DISTRIBUTION LIST

(REFERENCE: COMPANY PRACTICE 7-21-1)

REPORT TITLE

FINAL REPORT: EMPIRICAL EVALUATION OF PUMP INLET COMPLIANCE

REPORT NO.

ATR-73(7257)-1

PUBLICATION DATE

JULY 1972

SECURITY CLASSIFICATION

Unclassified

(NOTE: FOR OFF-SITE PERSONNEL, SHOW LOCATION SYMBOL, e.g. JOHN Q. PUBLIC/VAFB)

F. G. Ghahremani (15)

E. G. Hertler

J. H. Irving

T. Iura

V. H. Monteil

J. G. Payne

F. R. Reilly

S. Rubin (10)

W. P. Targoff

W. A. Ufford

R. G. Wagner

J. G. Wilder

APPROVED BY

DATE

SHEET 1 OF 1

THE AEROSPACE CORPORATION

EXTERNAL DISTRIBUTION LIST

(REFERENCE: COMPANY PRACTICE 7-21-1)

REPORT TITLE

FINAL REPORT: EMPIRICAL EVALUATION OF PUMP INLET COMPLIANCE

REPORT NO.

ATR-73(7257)-1

PUBLICATION DATE

JULY 1972

SECURITY CLASSIFICATION

Unclassified

(NOTE: SHOW FULL MAILING ADDRESS; INCLUDE ZIP CODE, MILITARY OFFICE SYMBOL, AND "ATTENTION" LINE.)

Aerojet-General Corporation
P. O. Box 1947
Technical Library, Bldg. 2015, Dept. 2410
Sacramento, CA 95809
Attn: R. Stiff (1 cy)

Aerojet Liquid Rocket Co.
P. O. Box 13222
Sacramento, CA 95813
Attn: Mr. K. P. Collins (1 cy)
Asst; Program Mgr., Bldg. 2025, Dept. 9800

Air Force Rocket Propulsion Laboratory
Research and Technology Division
Air Force Systems Command
Edwards, CA 93523
Attn: RPRPD/Mr. H. Main (1 cy)

Bellcomm
955 L'Enfant Plaza, S. W.
Washington, DC 20022
Attn: H. S. London (1 cy)

Boeing Company
1625 K Street, N. W.
Washington, DC 20006
Attn: Library (1 cy)

Boeing Company
P. O. Box 1470
Huntsville, AL 35807
Attn: Maxie Brown, Space Shuttle (1 cy)

CCSD
Michoud Operation
P. O. Box 29200
New Orleans, LA 70129
Attn: Mr. C. E. Tharrott, Dept. 2760 (1 cy)

Defense Documentation Center Headquarters
Cameron Station, Bldg. 5
5010 Duke Street
Alexandria, VA 22314
Attn: TISIA (1 cy)

Chrysler Corporation
Missile Division
P. O. Box 2628
Detroit, MI 48231
Attn: John Gates (1 cy)

General Dynamics, Convair Division
Library & Information Services (128-00)
P. O. Box 1128
San Diego, CA 93112
Attn: Frank Dore (1 cy)

Grumman Aerospace Corporation
Plant 25 - Space Shuttle
Bethpage, L.I., NY 11714
Attn: Mr. Fred Raymer (1 cy)

Jet Propulsion
4800 Oak Grove Drive
Pasadena, CA 91103
Attn: Mr. Robert Rose (1 cy)
Attn: Mr. Louis Toth (2 cys)
Attn: Mr. D. D. Lawson, Technical Monitor
(1 cy)

IF LIST COMPRISES TWO OR MORE SHEETS, COMPLETE
THIS SIGNATURE BLOCK ON LAST SHEET ONLY

APPROVED BY _____

(FOR AEROSPACE CORPORATION)

DATE _____

APPROVED BY _____

(FOR COGNIZANT AF OFFICE)

(SYMBOL)

DATE _____

THE AEROSPACE CORPORATION

EXTERNAL DISTRIBUTION LIST

(REFERENCE: COMPANY PRACTICE 7-21-1)

REPORT TITLE

FINAL REPORT: EMPIRICAL EVALUATION OF PUMP INLET COMPLIANCE

REPORT NO.
ATR-73(7257)-1

PUBLICATION DATE
JULY 1972

SECURITY CLASSIFICATION
Unclassified

(NOTE: SHOW FULL MAILING ADDRESS; INCLUDE ZIP CODE, MILITARY OFFICE SYMBOL, AND "ATTENTION" LINE.)

NASA Pasadena Office
4800 Oak Grove Drive
Pasadena, CA 91103
Attn: Patents & Contracts Management (1 cy)

Lockheed Missiles and Space Company
P. O. Box 504
Sunnyvale, CA 94088
Attn: J. Guill, Technical Information Center (1 cy)
Attn: John Lloyd (1 cy)
Manager, Alternate Space Shtl Concept Study
Dept. G1-51, Bldg. 538

McDonnell Douglas Astronautics Company
Missile and Space Systems Division
3000 Ocean Park Blvd.
Santa Monica, CA 90406
Attn: Mr. R. W. Hallet (1 cy)
Chief Engineer
Adv. Space Tech.

McDonnell Douglas Astronautics Company
P. O. Box 516
St. Louis, MO. 63166
Attn: Mr. Sherman L. Hislop (1 cy)
Director of Booster/Orbiter Integration

Pratt & Whitney Aircraft Corp.
P. O. Box 2691
West Palm Beach, FL 33402
Attn: W. E. Young (1 cy)
Attn: William Crescine (1 cy)

Rocketdyne/North American Rockwell Corp.
6633 Canoga Avenue
Canoga Park, CA 91304
Attn: Mr. J. E. Hale, Project Engr.,
Mail Code AA72 (1 cy)
Attn: Dr. Eugene Jackson, Dept. 596-115,
AC51 (1 cy)
Attn: Dr. R. J. Thompson (1 cy)
Attn: Mr. S. F. Iacobellis (1 cy)
Attn: Library (1 cy)

North American Rockwell Corporation
Space Division
12214 Lakewood Blvd.
Downey, CA 90241
Attn: Mr. B. Hello (1 cy)
Vice President Corporate Wide General
Manager - Space Shuttle Program
Attn: Mr. Joe Monroe (1 cy)
Attn: Library (1 cy)

Space and Missile Systems Organization
Air Force Unit Post Office
Los Angeles, CA 90045
Attn: Colonel Clark, Technical Data Center
(1 cy)

Scientific and Technical Information Facility
P. O. Box 33
College Park, MD 20740
Attn: NASA Representative, Code CRT (20 cys)

IF LIST COMPRISES TWO OR MORE SHEETS, COMPLETE
THIS SIGNATURE BLOCK ON LAST SHEET ONLY

APPROVED BY _____ (FOR AEROSPACE CORPORATION)	DATE _____
APPROVED BY _____ (FOR COGNIZANT AF OFFICE)	DATE _____ (SYMBOL)

THE AEROSPACE CORPORATION

EXTERNAL DISTRIBUTION LIST

(REFERENCE: COMPANY PRACTICE 7-21-1)

REPORT TITLE

FINAL REPORT: EMPIRICAL EVALUATION OF PUMP INLET COMPLIANCE

REPORT NO.
ATR-73(7257)-1

PUBLICATION DATE
JULY 1972

SECURITY CLASSIFICATION
Unclassified

(NOTE: SHOW FULL MAILING ADDRESS; INCLUDE ZIP CODE, MILITARY OFFICE SYMBOL, AND "ATTENTION" LINE.)

TRW, Inc.
TRW Systems Group
One Space Park
Redondo Beach, CA 90278
Attn: G. W. Elverum (1 cy)

NASA Headquarters
Washington, DC 20546
Attn: MT/Director, Advanced Manned Missions (1 cy)
Office of Manned Space Flight
Attn: Contracting Officer (1 cy)
Attn: RPL/Chief, Liquid Propulsion Technology (3 cy)
Office of Advanced Research and Technology
Washington, DC 20546
Attn: Director, Technology Utilization Div. (1 cy)
Office of Technology Utilization
Attn: SV/Director, Launch Vehicles & Propulsion
(1 cy)
Office of Space Science and Applications

NASA/Langley Research Center
Hampton, VA 23365
Attn: 01.000/Director (1 cy)
Attn: 213/Dr. Robert Levine (1 cy)

NASA/Lewis Research Center
21000 Brookpark Road
Cleveland, OH 44135
Attn: 0100/Director (1 cy)
Attn: Mr. Howard Douglas (1 cy)
Attn: Office of Technical Information (1 cy)
Attn: MS5-9/W. R. Britsch (1 cy)

NASA/Manned Spacecraft Center
Houston, TX 77058
Attn: J. G. Thibodaux, Jr. (1 cy)
Chief, Prop. & Power Div.
Attn: EF2/Mr. Cecil Gibson (1 cy)
Attn: Office of Technical Information (1 cy)

NASA/Marshall Space Flight Center
Marshall Space Flight Center, AL 35812
Attn: A&TS-TU (1 cy)
A&TS-MS-IL (1 cy)
A&TS-MS-I/Mr. S. Fraage (1 cy)
A&TS-MS-IP (2 cys)
S&E-ASTN-X/Mr. Jerry Thomson (1 cy)
S&E-ASTN-RR/Mr. B. R. Birdwell (1 cy)
S&E-ASTN-P/Mr. H. G. Paul (1 cy)
S&E-ASTN-PJ/Mr. H. Phillips (1 cy)
S&E-ASTN-PFB/Mr. R. Spink (20 cys)

Martin Marietta Corporation
P. O. Box 179
Denver, CO 80201
Attn: Mr. R. D. Vaage (1 cy)

IF LIST COMPRISES TWO OR MORE SHEETS, COMPLETE
THIS SIGNATURE BLOCK ON LAST SHEET ONLY

APPROVED BY <u>J. E. W. [Signature]</u> (FOR AEROSPACE CORPORATION)	DATE <u>9/5/72</u>
APPROVED BY _____ (FOR COGNIZANT A.F. OFFICE)	DATE _____ (SYMBOL)

SHEET 3 OF 3